Atypical cofilin signaling drives dendritic cell migration through the extracellular matrix via nuclear deformation

Warner, Harry; Franciosa, Giulia; van der Borg, Guus; Coenen, Britt; Faas, Felix; Koenig, Claire; de Boer, Rinse; Classens, René; Maassen, Sjors; Baranov, Maksim V

Published in:
Cell reports

DOI:
10.1016/j.celrep.2024.113866

Cell Reports

Article

Atypical cofilin signaling drives dendritic cell migration through the extracellular matrix via nuclear deformation

Graphical abstract

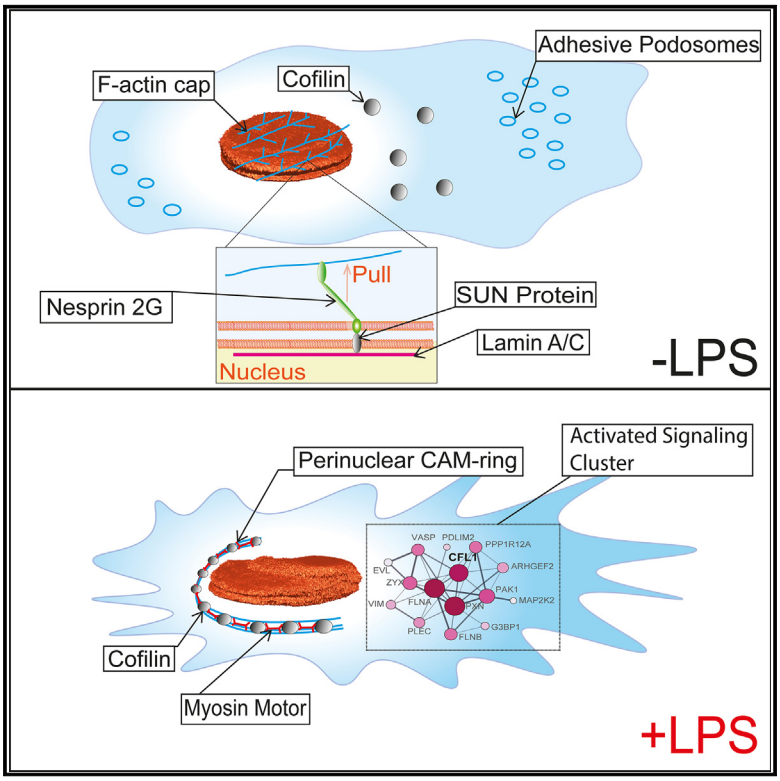

Authors

Harry Warner, Giulia Franciosa, Guus van der Borg, ..., Jesper Velgaard Olsen, Laia Querol Cano, Geert van den Bogaart

Correspondence

g.van.den.bogaart@rug.nl

In brief

Dendritic cells are the interface between the innate and the adaptive immune systems, which require them to migrate through complex 3D environments to reach lymph nodes. Warner et al. show that dendritic cells phosphorylate the actin regulator cofilin at serine 41 to better squeeze their nuclei through gaps in this complex environment.

Highlights

- Dendritic cells round their nuclei via adhesion loss when activated by LPS
- Activation enhances nuclear squeezing through the extracellular matrix
- The passage of the nucleus through the matrix requires actomyosin squeezing
- Perinuclear actomyosin assembly is driven by cofilin phosphorylation at serine 41

Warner et al., 2024, Cell Reports *43*, 113866
March 26, 2024
https://doi.org/10.1016/j.celrep.2024.113866

CellPress

Cell Reports

CellPress
OPEN ACCESS

Article

Atypical cofilin signaling drives dendritic cell migration through the extracellular matrix via nuclear deformation

Harry Warner,[1] Giulia Franciosa,[2,8] Guus van der Borg,[3,8] Britt Coenen,[1] Felix Faas,[1] Claire Koenig,[2] Rinse de Boer,[1] René Classens,[4] Sjors Maassen,[1] Maksim V. Baranov,[1] Shweta Mahajan,[1] Deepti Dabral,[1] Frans Bianchi,[1] Niek van Hilten,[5] Herre Jelger Risselada,[5,6] Wouter H. Roos,[3] Jesper Velgaard Olsen,[2] Laia Querol Cano,[4] and Geert van den Bogaart[1,7,9,*]

[1]Department of Molecular Immunology, Groningen Biomolecular Sciences and Biotechnology Institute, University of Groningen, Groningen, the Netherlands
[2]Novo Nordisk Foundation Center for Protein Research, Faculty of Health and Medical Sciences, University of Copenhagen, Copenhagen, Denmark
[3]Molecular Biophysics, Zernike Institute for Advanced Materials, University of Groningen, Groningen, the Netherlands
[4]Department of Medical BioSciences, Radboud University Medical Center, Nijmegen, the Netherlands
[5]Leiden Institute of Chemistry, Leiden University, Leiden, the Netherlands
[6]Department of Physics, TU Dortmund, Dortmund, Germany
[7]Department of Pathology and Medical Biology, University Medical Center Groningen, Groningen, the Netherlands
[8]These authors contributed equally
[9]Lead contact
*Correspondence: g.van.den.bogaart@rug.nl
https://doi.org/10.1016/j.celrep.2024.113866

SUMMARY

To mount an adaptive immune response, dendritic cells must migrate to lymph nodes to present antigens to T cells. Critical to 3D migration is the nucleus, which is the size-limiting barrier for migration through the extracellular matrix. Here, we show that inflammatory activation of dendritic cells leads to the nucleus becoming spherically deformed and enables dendritic cells to overcome the typical 2- to 3-μm diameter limit for 3D migration through gaps in the extracellular matrix. We show that the nuclear shape change is partially attained through reduced cell adhesion, whereas improved 3D migration is achieved through reprogramming of the actin cytoskeleton. Specifically, our data point to a model whereby the phosphorylation of cofilin-1 at serine 41 drives the assembly of a cofilin-actomyosin ring proximal to the nucleus and enhances migration through 3D collagen gels. In summary, these data describe signaling events through which dendritic cells deform their nucleus and enhance their migratory capacity.

INTRODUCTION

Dendritic cells form the interface between the innate and the adaptive immune systems and operate throughout the body in environments with very different stiffnesses. Before activation, dendritic cells reside in virtually all tissues, where they adapt to the local biochemical and physical cues provided by surrounding cells and the extracellular matrix (ECM).[1–4] Therefore, dendritic cells must be extremely plastic in their mechanosensing behavior, being able to function at stiffnesses ranging from <1 kPa (e.g., brain) to >10 kPa (e.g., muscle). Moreover, following the recognition and ingestion of a pathogen, dendritic cells become activated and rapidly migrate to a local lymph node to activate T cells. To facilitate this migration and adapt to the physiological properties of lymph nodes, activated dendritic cells undergo both rapid and systematic reprogramming of their adhesion machinery, breaking down podosomes and becoming less adhesive.[5] Furthermore, once at a lymph node, dendritic cells stimulate fibroblasts to trigger lymph node expansion.[6,7] Lymph node expansion drives stiffening of the lymph node and prevents crowding of lymphocytes within the lymph node, a mechanical event that dendritic cells have to adapt to as well.[8]

Cell-matrix adhesion is critical to most metazoan life.[9] In particular, modifications to cell-matrix adhesion efficiency via cell spreading are known to be far reaching, regulating not only cell shape, but also gene expression and cell differentiation.[10–14] Furthermore, forces from the ECM are known to be transmitted by the actin cytoskeleton to the nucleus via LINC (linker of nucleoskeleton and cytoskeleton) complexes.[15–19] This can regulate nuclear morphology (with the nucleus getting more spherical as adhesion reduces) and has even been reported to regulate cell differentiation.[13] Furthermore, multiple studies have indicated that dendritic cell migration can occur in the absence of integrin-based adhesion machinery,[20,21] and numerous results have indicated that activated dendritic

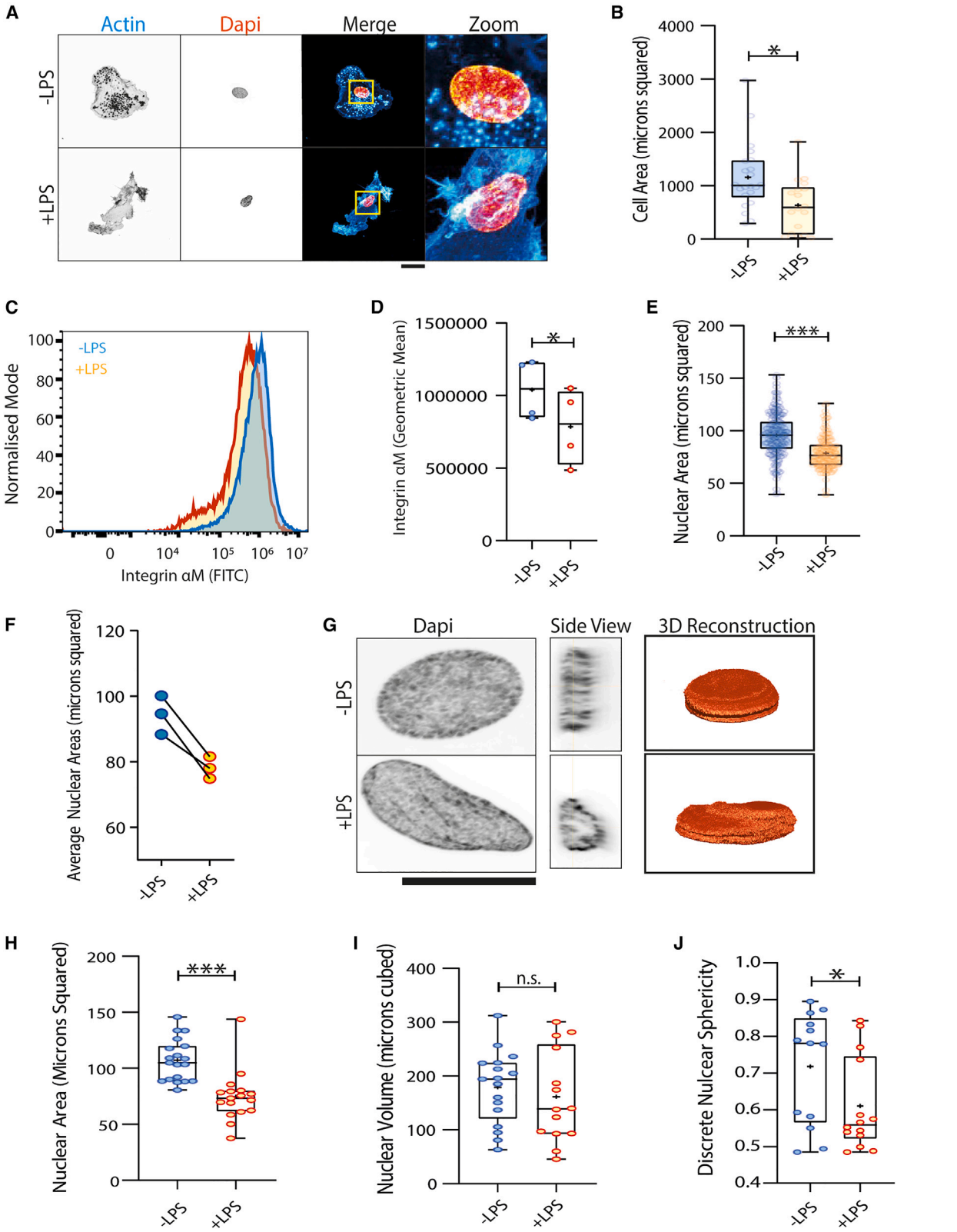

(legend on next page)

cells indeed switch to a less adhesive migratory phenotype.[5,22] Therefore, it seems possible that reduced force transmission from the ECM to the dendritic cell nucleus may occur following inflammatory activation.

Critical to both 3D migration and mechanosensing is the nucleus. During migration, the nucleus is used by cells to probe gap sizes in the ECM, transmit signals of confinement to the actin cytoskeleton, and generate intracellular pressure.[23–26] Nesprin-2G-based LINC complexes connect the actin cytoskeleton, via Nesprin-2G and SUN proteins, to lamin filaments, enabling the cell to pull the nucleus through gaps in the ECM and mechanoregulate the genome.[27–30] Furthermore, the nucleus is known to act as a size-limiting organelle, blocking migration of mononuclear cells (including dendritic cells) through ECM gaps with diameters smaller than about 2–3 μm.[31–33] While the role of the nucleus in dendritic cell migration is well defined, how the dendritic cell nucleus senses force when tissue-resident is poorly understood, as is the effect of inflammatory activation on the nucleus in the context of 3D migration.

Here, using quantitative microscopy, we demonstrate that dendritic cell activation leads to a change in nuclear morphology and enhanced passage of the nucleus (and thus the whole cell) through 2-μm-diameter pores. While activation-induced de-adhesion can explain the change in dendritic cell nuclear morphology, it cannot explain the increased migration efficiency, as atomic force microscopy (AFM) measurements indicate that the bulk nucleus does not become softer in response to inflammatory stimulation. Instead, we demonstrate, using phosphoproteomics and quantitative microscopy, that cofilin-1 is phosphorylated at serine 41 in response to inflammatory activation, and this seems to promote the assembly of a contractile cofilin-actomyosin (CAM) ring proximal to the nucleus. This phosphorylation of cofilin-1 at serine 41 seems to enhance nuclear squeezing and increases migration efficiency through the ECM.

RESULTS

As inflammatory activation has long been known to reduce dendritic cell adhesion in response to lipopolysaccharide (LPS),[5,22] it is logical that activation may concomitantly alter the shape of the dendritic cell nucleus. Therefore, to examine how inflammation-induced de-adhesion influences the dendritic cell nucleus, we differentiated monocyte-derived dendritic cells (moDCs) from human peripheral blood monocytes, stimulated them with bacteria-derived LPS overnight (18–24 h), and quantified the z-projected area of complete moDCs (Figures 1A and 1B). This revealed that, consistent with previous results, in the x-y plane of the cell, moDCs become less spread[5,22] (Figure 1B). Furthermore, flow cytometry analysis of moDCs revealed that the αM integrin (found in podosomes[32]) is downregulated following inflammatory activation (Figures 1C and 1D). The z-projected area of moDC nuclei was also reduced following overnight LPS (Figure 1E). This effect was consistently observed for all three donors assessed (Figure 1F; Table S5). Through the use of 3D Airyscan superresolution microscopy, we measured the approximate volume of nuclei from inactivated and activated moDCs (Figures 1G and 1H). This revealed that, although the nuclei get smaller in the projected x-y plane upon activation (Figure 1H), they maintain a constant volume (Figure 1I) and extend into the z plane (herein referred to as "nuclear deformation"). We also performed a more advanced analysis of the nuclear morphology from the high-resolution Airyscan microscopy z stacks; the discrete sphericity of moDC nuclei decreased in response to LPS stimulation (Figure 1J).

We also examined the effect of LPS stimulation on $CD14^+$ monocyte-derived macrophages (Figures S1A and S1B). We compared macrophages with moDCs, because, in contrast to dendritic cells, the activation of macrophages by inflammatory stimuli does not result in their migration to the lymph nodes. However, we found that the z-projected area of the nuclei of macrophages became larger. We also verified that the same nuclear deformation occurs in moDCs in response to *Escherichia coli* exposure (Figures S1C and S1D).

We also confirmed that macrophages do not contaminate our moDC cultures: primary monocytes are relatively uncontaminated by cells expressing macrophage markers (Figures S1E–S1H). Furthermore, stimulation of moDCs with LPS did not largely affect seeding density (Figure S1I), meaning that activation does not bias the results toward more adherent contaminant cells.

We hypothesized that activation-associated changes to the nucleus facilitate more efficient migration through gaps in the

Figure 1. LPS stimulation spherically deforms the dendritic cell nucleus

(A) Confocal micrographs of moDCs. Scale bar, 20 μm.

(B) Quantification of z-projected cellular area (cell spreading) (data points represent individual cells pooled from three donors, minimum 39 measurements per condition).

(C) Example flow cytometry histogram of the expression of the αM integrin subunit.

(D) Quantification of the geometric mean fluorescence intensity from (C) of the αM integrin staining in moDCs cultured ± LPS. Data points represent donor averages from four donors.

(E) Quantification of z-projected nuclear area (data points represent individual cells pooled from three donors, minimum 157 measurements per condition).

(F) Donor-specific changes (from E) in average z-projected nuclear area. Data points represent donor averages from three donors. Statistics for individual donors are in Table S5.

(G) Airyscan and 3D reconstruction of dendritic cell nuclei. Scale bar, 10 μm.

(H and I) (H) Quantification of z-projected nuclear size of (G) and (I) quantification of nuclear volume (of the same nuclei) (data points represent individual cells pooled from four donors, at least 14 measurements per condition).

(J) Quantification of the discrete sphericity of dendritic cell nuclei. Data points represent individual cells pooled from four donors. Statistical significance was calculated using two-tailed unpaired (for comparison of individual cells) or paired (for comparison of donor averages) t tests (selected according to the distribution pattern of the data). *$p < 0.05$; ***$p < 0.001$; n.s., not significant. For box-and-whisker plots, box represents 25th to 75th percentile, whiskers represent maximum and minimum values, middle band represents data median, and + represents data mean.

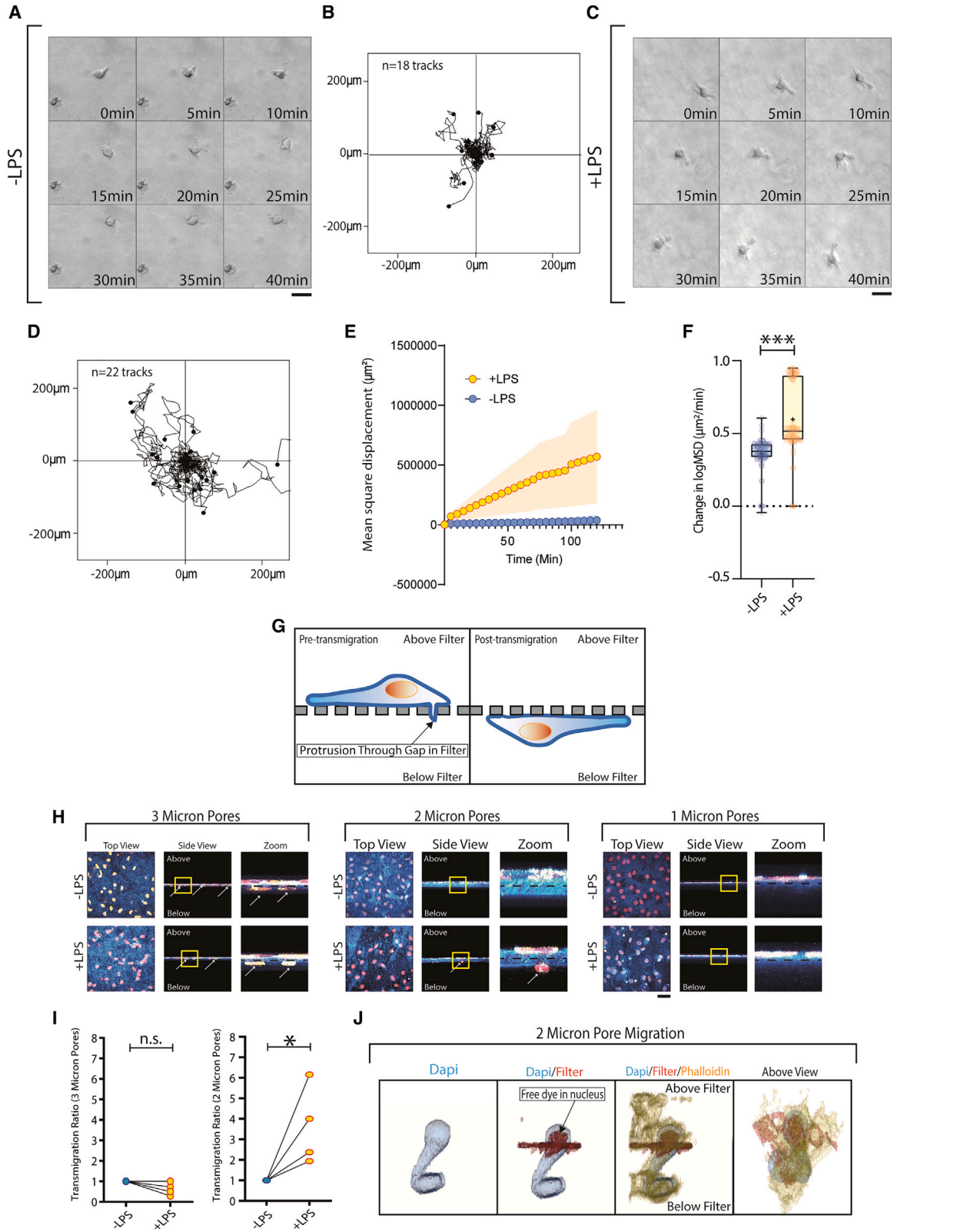

(legend on next page)

ECM, as activated dendritic cells migrate to lymph nodes, whereas macrophages do not. We first confirmed that activation increases moDC migration efficiency in a 3D matrix. To do this, we embedded inactive and LPS-stimulated moDCs into 3D bovine dermal collagen (concentration of 1.7 mg mL^{-1}). Previous work has demonstrated that a 3D matrix made of bovine dermal collagen at this concentration has pore diameters of ~2–6 μm (i.e., approaching the size limit for 3D migration as determined by the nucleus).[31] Indeed, Wolf et al.[31] utilized this approach to test the impact of matrix dimensions on metalloproteinase-independent 3D migration. However, as we cannot simultaneously measure pore size and migration efficiency, we selected mean square displacement (MSD) as our principal metric of interest, as this determines confinement of a particle (i.e., a moDC) within a closed environment (i.e., the collagen gel) (Figures 2A–2F; Videos S1 and S2). This confirmed that inflammatory activation reduces the confining effect of 3D collagen on moDCs, as the MSD substantially increased in activated moDCs compared with inactive moDCs (Figure 2F).

To test more directly the contribution of the nucleus to this increased MSD, we utilized a previously developed approach.[31,32] Specifically, moDCs were seeded onto polycarbonate filters coated with fluorescently labeled gelatin with defined pore diameters of 1, 2, 3, and 8 μm, in the absence and presence of LPS (Figure 2G). These pore diameters were selected as the nucleus typically limits migration through ECM gaps that are smaller than 3 μm.[31,32] Consistent with previous work,[32,33] in the absence of LPS, moDCs were able to migrate through 3-μm pores but were largely blocked from migrating through 2-μm pores and completely blocked from migrating through 1-μm pores. However, LPS-stimulated moDCs were able to migrate with far greater efficiency through 2-μm pores, but were still blocked from migrating through 1-μm pores (Figures 2H–2J**)**. Although the relative increase in migration efficiency through 2-μm pores (comparing with vs. without LPS) was consistent among donors, the overall efficiency of localized transmigration through both 2- and 3-μm pores was highly variable; the values ranged from 1% to more than 40%, depending on the donor and the filter (Table S1). Control experiments using filters with 8-μm-diameter holes showed that, although LPS did not consistently affect the migration efficiency (Figures S1J and S1K), the levels of variability among donors were similarly high compared with the smaller pore sizes (Table S1). Thus, the difference in migration capacity likely reflects donor variation.

We also verified that changes to the nucleus are not due to the biochemical input of the ECM by seeding moDCs on coverslips coated with different ECM components (collagen, fibronectin, laminin, vitronectin, or fibrinogen) ±LPS (Figures S2A–S2J). This indicated that the biochemical input of most of these ECM components (except laminin) does not have an impact on moDC nuclear morphology or LPS-induced deformation.

To verify that nuclear deformation is at least partially due to reduced moDC adhesion and to confirm that this change can occur at physiological stiffnesses, we examined the morphology of moDC nuclei, with and without LPS, cultured on fibronectin gels with set stiffness values. These stiffnesses ranged from 10 through 5 to 1 kPa. These values were selected to broadly reflect the stiffness of tissues ranging from muscle to liver, respectively. The z-projected nuclear areas of the inactive moDCs continued to get smaller (resembling activated nuclei in moDCs cultured on glass) as the substrate became softer until they reached the 1-kPa gel, at which point they became larger (Figures 3A and 3B). Activation with LPS reduced the z-projected area of the nuclei, relative to inactive moDCs, on both glass and 10-kPa matrix, but failed to show a difference on 5-kPa and softer matrices. These results imply that the deformation of the nucleus in response to LPS is due to reduced moDC adhesion and demonstrate that the difference between inactive and active moDC nuclei may be observed *in vivo* (Figures 3A and 3B).

As LPS-stimulation-induced nuclear deformation is dependent on alterations to the cell's adhesive properties, we hypothesized that activation may alter mechanical forces across actin-based LINC complexes. To examine actin-based LINC complexes, we used the Nesprin-2 tension probe mN2G-TS.[34] This probe has an internal mTFP-Venus donor/acceptor Förster resonance energy transfer (FRET) pair, which is pulled apart as mechanical tension across the protein increases (Figure 3C).[34] The mN2G-TS probe revealed a reduction in mechanical tension across Nesprin-2-based LINC complexes in response to LPS

Figure 2. LPS stimulation enhances nuclear squeezing through the ECM

(A) Stills from representative time-lapse microscopy of an inactive dendritic cell migrating in collagen. Scale bar, 20 μm.

(B) Example migration traces of inactive dendritic cells.

(C) Stills from representative time-lapse microscopy of an LPS-activated dendritic cell migrating in collagen. Scale bar, 20 μm.

(D) Example migration traces of LPS-activated dendritic cells.

(E) Example mean square displacements of inactive (−LPS) and active (+LPS) dendritic cells migrating in collagen. Shaded region represents SEM.

(F) Quantification of rate of mean square displacement (MSD) for inactive and active dendritic cells (data points represent individual cells pooled from three donors, 90 measurements per condition).

(G) Schematic demonstrating filter experiment setup. Dendritic cells are seeded on top of gelatin-coated polycarbonate filters with 1-, 2-, 3-, or 8-μm pore diameters.

(H) Confocal micrographs of dendritic cells cultured on gelatin-coated polycarbonate filters with set pore diameters (fluorescent gelatin in blue, DAPI in red). Black dashed line indicates approximate position of the polycarbonate filter. Scale bar, 40 μm.

(I) Quantification of the normalized transmigration ratio of dendritic cells through 3- and 2-μm pore diameters (defined as the number of cells passing through the filter normalized to local seeding density). Data for four donors. Data for 8-μm pore size are in Figures S1J–S1K.

(J) A 3D reconstruction of a dendritic cell observed migrating through a 2-μm-diameter pore. Free dye in the nucleus originates from the fluorescently labeled gelatin used to coat the polycarbonate filter. Statistical significance was calculated using two-tailed unpaired (F) or paired (I) t tests (selected according to distribution pattern of the data). *$p < 0.05$; ***$p < 0.001$; n.s., not significant. For box-and-whisker plots, box represents 25th to 75th percentile, whiskers represent maximum and minimum values, middle band represents data median, and + represents data mean.

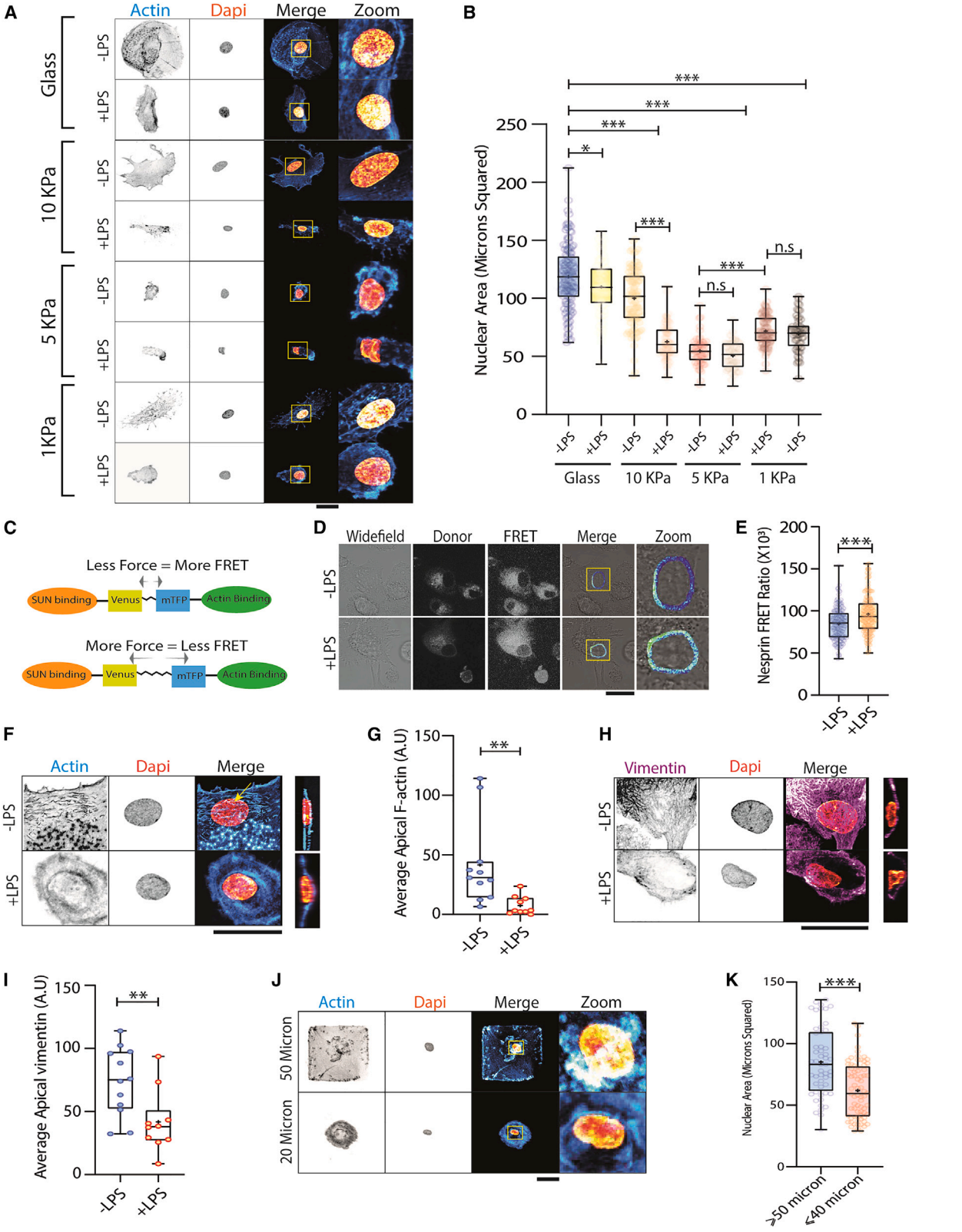

(legend on next page)

(Figures 3D and 3E). We verified the accuracy of the probe by comparing the FRET ratio produced by the WT probe to the headless Nesprin-2 tension probe, which is unable to connect to the actin cytoskeleton, resulting in maximum FRET[34] (Figures S3A and S3B).

Consistent with these FRET data, Airyscan microscopy revealed the presence of a previously observed[35,36] actin cap positioned close to the nucleus that breaks down in response to LPS stimulation (Figures 3F and 3G). To characterize this actin cap further, we examined the intermediate filament vimentin, as this has been shown to support the nucleus in moDCs and is supported by the F-actin cytoskeleton.[37–40] Vimentin also showed a reduced intensity above the nucleus in response to LPS (Figures 3H and 3I). We also examined the microtubule cytoskeleton (Figures S3C and S3D). We observed a slight, but non-significant, reduction in the association of microtubules with the nucleus in response to LPS.

To confirm the contribution of actin-dependent adhesion on the shape of the nucleus, we cultured moDCs on micropatterned substrates with defined adhesion areas. We observed a clear distinction in z-projected nucleus size between cells cultured with adhesion areas of $\geq$50 μm and those forced to adhere on areas of $\leq$40 μm (Figures 3J and 3K). We further confirmed these results by culturing moDCs in the presence of the actin polymerization inhibitor latrunculin B or cytochalasin D for 1 h (Figures S3E and S3F).

We also verified the effect of moDC activation on the expression and/or localization of lamin-A/C, which has been shown to alter with tissue stiffness[29,41] and has been shown to turn over less rapidly in activated moDCs.[42] Using confocal microscopy, we were unable to observe a difference in lamin-A/C (both isoforms are recognized by the antibody) wrinkling in response to LPS stimulation (Figures S3G and S3H). Through western blotting we observed that lamin-C is the predominant isoform expressed in moDCs, which showed a slight, non-significant reduction in expression in response to LPS stimulation (Figures S3I–S3J). Therefore, we also examined the intensity of lamin-A/C staining at the nucleus using confocal microscopy (using a set laser power and exposure) (Figure S3K). Through this we observed that lamin-A/C levels decrease in the nucleus (which may be too subtle to observe via western blot) in response to LPS-mediated activation. Either way, this alteration in lamin-A/C may further contribute to activation-induced nuclear deformation. Consistent with this, we observed that overexpression of lamin-A/C in moDCs blocks the reduction in x-y nuclear size that accompanies moDC activation (Figure S3L and S3M).

As moDC activation drives nuclear spherical deformation, we examined the biophysical properties of moDC nuclei. We first examined the fluidity of the moDC membrane using the molecular rotor BODIPY-C10 FRET-FLIM dye (Figures 4A–4C)[43] to analyze the lifetime of the dye at the nuclear rim, as previously described.[29] This suggested that the fluidity of the nucleus increases in response to LPS stimulation and may promote the flow of the nuclear envelope through the ECM. Indeed, analyzing the lifetime of the BODIPY-C10 away from the nucleus did not reveal the same change (Figure 4D), suggesting this increase in fluidity is nucleus specific.

To examine bulk nuclear dynamics, we live-imaged the moDC nucleus with Airyscan microscopy, using Hoechst, under ±LPS conditions (Figures 4E and 4F; Videos S3 and S4). This revealed that the bulk nucleus fluctuations, as measured by Hoechst staining within the nucleus, increase in LPS-activated moDCs compared with inactive moDCs. This dynamic behavior may explain how the activated moDC is better able to pass the bulk nuclear content through small gaps in the ECM. However, based on these data it is unclear if the nucleus is passively becoming more deformable (i.e., softer) via a reduction in actin-based adhesion and/or if it is being actively remodeled by the actin cytoskeleton.

To test if the moDC nucleus becomes more passively deformable in response to inflammatory activation, we performed AFM on moDCs to biophysically characterize the deformability of the bulk nucleus (i.e., the nuclear membrane and the chromatin).[44] This methodology has previously been used to characterize the moDC plasma membrane[45] as well as the nuclei of numerous cell types, including epithelial cells and fibroblasts.[29,35,46] Based on the increased migration efficiency of moDCs in response to LPS stimulation, we predicted that the nucleus

Figure 3. LPS stimulation drives nuclear deformation through adhesion loss

(A) Confocal micrographs of moDCs cultured overnight on substrates of various stiffnesses. Scale bar, 20 μm.

(B) Quantification of the z-projected nuclear areas, in the absence or presence of LPS, in dendritic cells cultured on substrates of various stiffnesses (data points represent individual cells pooled from four donors, minimum of 44 measurements per condition).

(C) Schematic of the Nesprin-2 FRET sensor.

(D) Example ratiometric FRET image of Nesprin-2 probe expressed in moDCs (3 h plus). Scale bar, 20 μm.

(E) Quantification of FRET ratio at the dendritic cell nuclear membrane (data points represent individual cells pooled from four donors, 156 measurements per condition).

(F) Airyscan images of F-actin (phalloidin, cyan in merge) around the dendritic cell nucleus in the absence or presence of LPS (overnight stimulation). Orange, DAPI. Yellow arrow indicates the nuclear F-actin cap. Scale bar, 20 μm.

(G) Quantification of average F-actin intensity above dendritic cell nuclei (data points represent individual cells pooled from three donors, at least 10 measurements per condition).

(H) Airyscan images of immunolabeled vimentin (magenta in merge) around the dendritic cell nucleus in the absence or presence of LPS. Scale bar, 20 μm.

(I) Quantification of average vimentin intensity above dendritic cell nuclei (data points represent individual cells pooled from three donors, at least 10 measurements per condition).

(J) Example images of dendritic cells cultured on micropatterned surfaces. Scale bar, 20 μm

(K) Quantification of the z-projected nuclear areas of dendritic cells cultured on areas of $\geq$50 μm or $\leq$40 μm (data points represent individual cells pooled from four donors, minimum of 52 measurements per condition). Statistical significance calculated using a two-tailed unpaired t test for two-condition experiments or ANOVA/Tukey's multiple comparisons test for experiments with three or more conditions (with test selected according to the distribution pattern of the data). *$p < 0.05$; **$p < 0.01$; ***$p < 0.001$; n.s., not significant. Error bars, SEM.

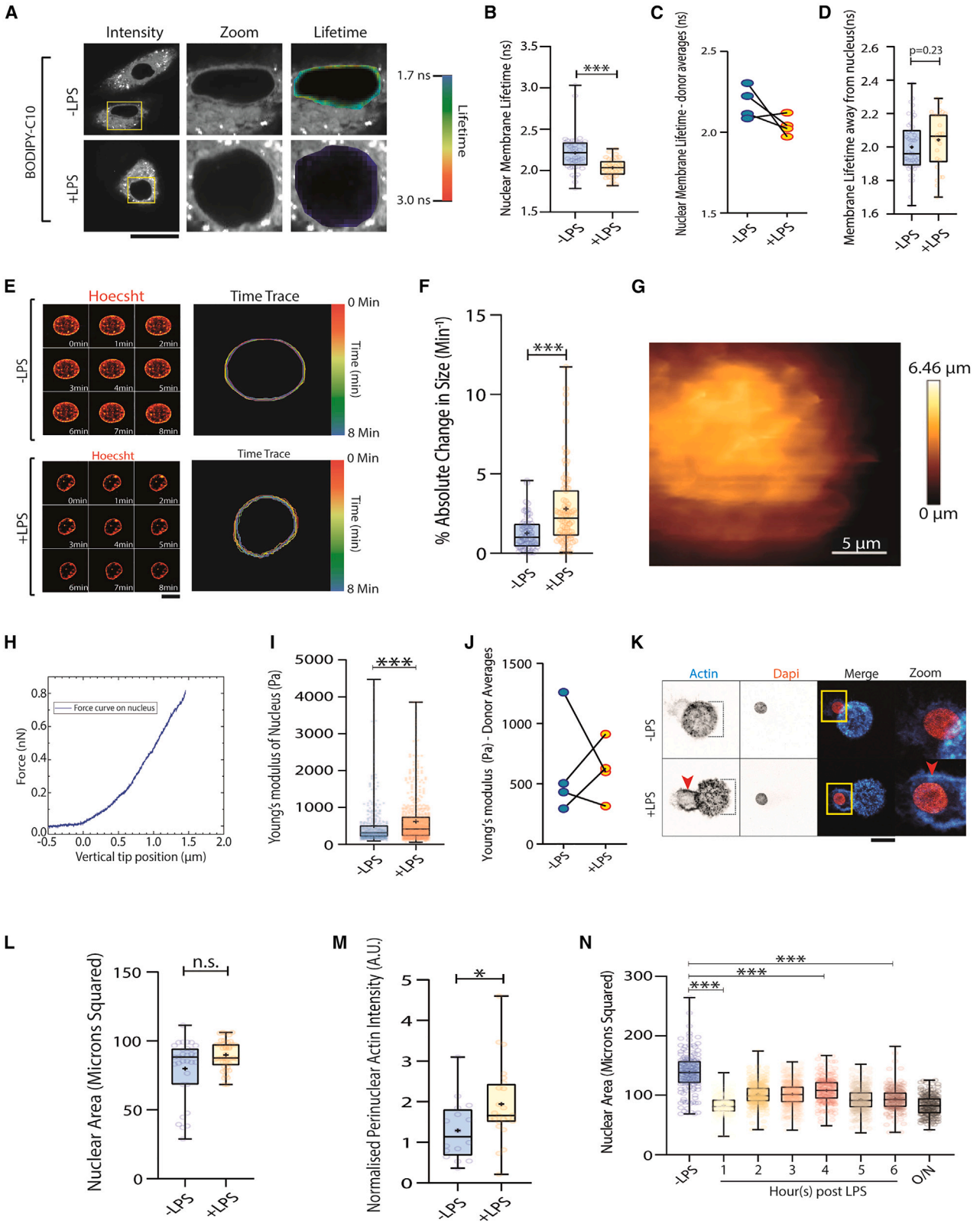

(legend on next page)

would soften upon LPS stimulation. Counter to our expectations, however, our AFM measurements showed that stimulating moDCs with LPS, on average, induced bulk nuclear stiffening (Figures 4G–4I). Although this effect was small and inconsistently observed among donors (Figure 4J; Table S5), these data suggest that activation-induced de-adhesion does not soften the moDC nucleus. Indeed, this is consistent with previous work that has shown that migration of moDCs through small gaps in the ECM depends on myosin activity to squeeze the nucleus.[47]

To further verify this hypothesis, we seeded moDCs ±LPS on disc micropatterns with adhesive diameters ranging from 10 to 20 μm. This enabled us to efficiently analyze the F-actin intensity at the plasma membrane region around the nucleus and whether the nucleus becomes more contractile in response to LPS.[47] While the nuclei did not show a significant change between without and with LPS on these micropatterns, we observed an increase in F-actin density at the cell rear plasma membrane (Figures 4K–4M). We therefore chose to do phosphoproteomics to better understand this F-actin assembly.

To select relevant time points of interest for (phospho)proteomic analysis, we first performed a time-course experiment, examining the shape of moDC nuclei every hour for 6 h following LPS stimulation (and following overnight stimulation). The time course revealed that the nucleus can shrink in the projected x-y plane within 1 h of LPS stimulation (i.e., the shortest time interval addressed), suggesting that the nucleus changes morphology in a (at least partially) transcription-independent manner (Figure 4N). Surprisingly, the size/shape of the nucleus continued to change over 6 h, partially restoring its projected size 4 h post-stimulation, before full deformation at the 6-h mark. Therefore, 1 and 4 h post-stimulation are ideal time points for identifying key signaling events that drive nuclear deformation; at both time points the nuclei are deformed relative to unstimulated moDCs, yet have slightly different shapes. Thus, by selecting these time points we could identify relatively stable signaling events that drive changes in the moDC nucleus at both 1 h and 4 h relative to inactive moDCs.

To identify early signaling events responsible for the observed changes in the actin cytoskeleton following LPS stimulation, we performed time-resolved mass spectrometry (MS)-based proteomics and phosphoproteomics on moDCs (Figure S4A; Tables S2 and S3). We compared the proteomes and phosphoproteomes of unstimulated moDCs with those stimulated for 1 and 4 h with LPS. The experiment was performed in six biological replicates (i.e., six different donors). Principal components analysis showed that samples clustered per condition, analyzing both the proteome and the phosphoproteome, indicating the reproducibility of the experiment (Figure S4B). On the phosphoproteome level, component 1 explained the difference between unstimulated and LPS-stimulated DCs, while on component 2, the differences between the time points are observed. On the full proteome level, the 1-h treatment condition resembled the unstimulated cells, while the 4-h treatment condition was the most different, consistent with phosphorylation being the fastest cellular event in the TLR4 signaling cascade. Proteomics revealed that 312 proteins, of 5,593 quantified, significantly changed in expression level over the time course analyzed (one-way ANOVA, false discovery rate [FDR] < 0.01) (Figure S4C). These proteins were involved in interferon signaling, cell adhesion, motility, and migration (Figure S4D).

Differential expression analysis of the phosphoproteomic data revealed 2,068 significantly regulated phosphosites (one-way ANOVA, FDR < 0.01). To systematically prioritize phosphosites for biological validation, we filtered out sites that were unlikely

Figure 4. LPS stimulation increases the stiffness of the bulk nucleus

(A) Intensity and fluorescence lifetime imaging microscopy (FLIM) examples of dendritic cells stained with BODIPY-C10. Scale bar, 20 μm.

(B) Quantification of BODIPY-C10 fluorescence lifetime at the nuclear envelope (data points represent individual cells pooled from four donors, minimum of 35 measurements per condition).

(C) Donor breakdown of BODIPY-C10 fluorescence lifetime averages at the nuclear envelope (from B). Data points represent donor averages for four donors. Statistics for individual donors are in Table S5.

(D) Quantification of BODIPY-C10 fluorescence lifetime away from the nuclear envelope (data points represent individual cells pooled from four donors, minimum of 26 measurements per condition).

(E) Airyscan microscopy movies of HOECHST-stained nucleus in dendritic cells. Scale bar, 10 μm.

(F) Quantification of absolute percentage changes in z-projected nuclear size over time (data points represent individual cells pooled from three donors, minimum of 67 measurements per condition).

(G) Scanning AFM image of dendritic cell nuclear pouch (a region in which the nucleus is stored).

(H) Example AFM indentation trace on dendritic cell nucleus.

(I) Young's modulus of dendritic cell nucleus quantification from AFM experiments (at least five cells per donor). Average value for −LPS is 506 Pa, average value for +LPS is 621 Pa. Error bars indicate standard error of the mean (−LPS = 28 Pa, +LPS = 24 Pa). Data points represent individual cells pooled from four donors, minimum 20 cells per condition. Statistics for individual donors are in Table S5.

(J) Donor breakdown of average Young's modulus of dendritic cell nucleus quantification from (H).

(K) Example images of dendritic cells cultured on disc-shaped micropatterned surfaces. Scale bar, 20 μm. Arrowhead shows perinuclear actin cable.

(L) Quantification of the z-projected nuclear areas of dendritic cells cultured on areas between 10 and 20 μm (data points represent individual cells pooled from three donors, minimum of 10 measurements per condition).

(M) Quantification of the normalized perinuclear actin intensity (data points represent individual cells pooled from three donors, minimum of five measurements per condition).

(N) Time-course data showing how the dendritic cell z-projected area changes over time after LPS, starting at 1 h (data points represent individual cells pooled from three donors, at least 145 measurements per condition). Statistical significance was calculated using two-tailed unpaired t tests for two-condition experiments or ANOVA/Tukey's multiple comparisons tests for experiments with three or more conditions (with test selected according to the distribution pattern of the data). A Kolmogorov-Smirnov test was used for AFM data to account for the large number of measurements. *$p < 0.05$; **$p < 0.01$; ***$p < 0.001$. Error bars, SEM. For box-and-whisker plots, box represents 25th to 75th percentile, whiskers represent maximum and minimum values, middle band represents data median, and + represents data mean.

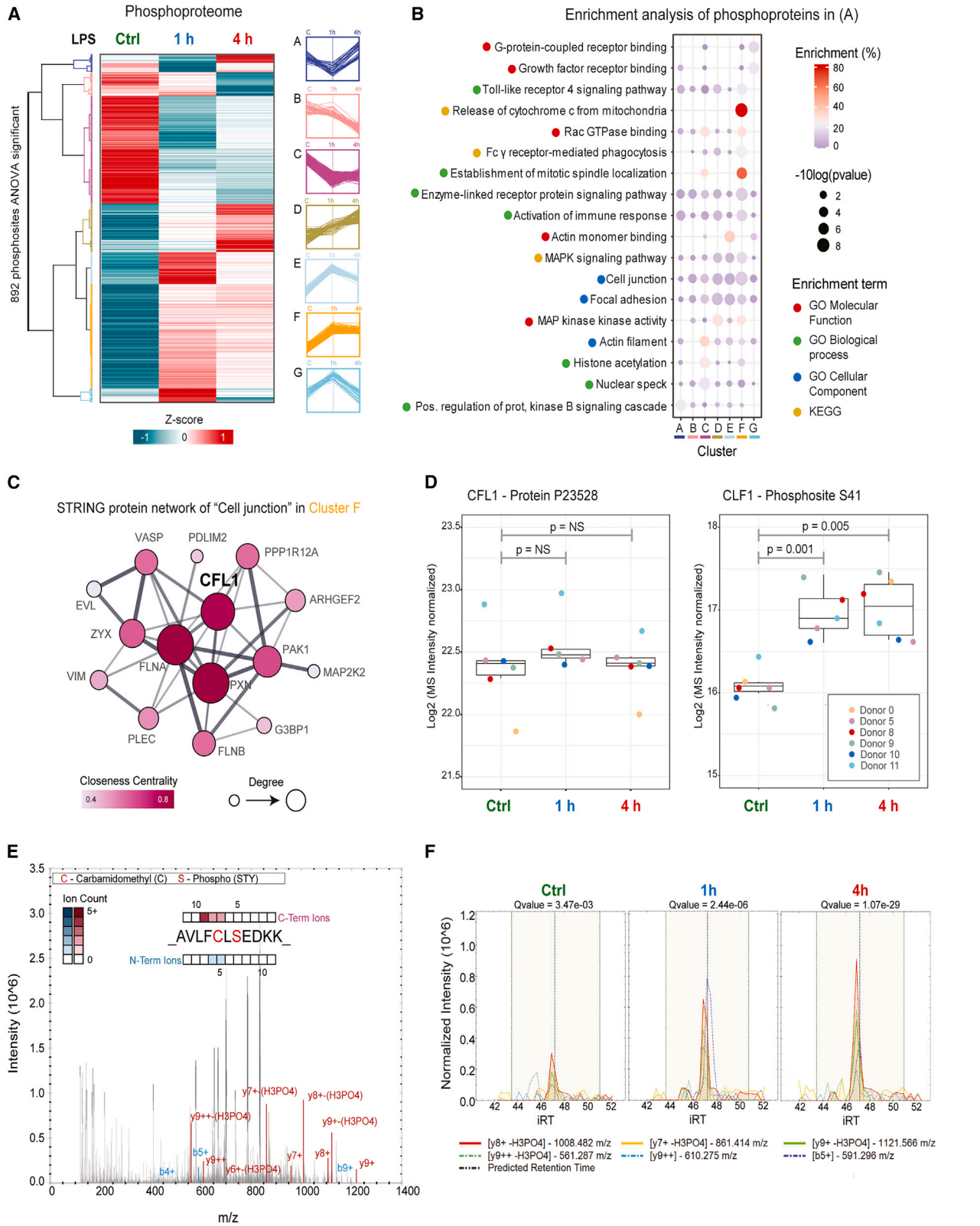

(legend on next page)

to have high biological relevance by filtering based on their "functional score."[48] This led to a list of 892 potential phosphosite candidates, which were used to perform hierarchical clustering to determine the directionality of the regulation upon LPS stimulation (Figure 5A). This analysis identified seven expression clusters. Gene ontology (GO) enrichment and pathway analysis on each expression cluster revealed that the major biological functions associated with LPS stimulation were related to inflammation (e.g., Toll-like receptor signaling pathway and activation of immune response) and cytoskeleton (e.g., actin filament and focal adhesion), enhancing our confidence in the dataset (Figure 5B). As we observed nuclear deformation at both 1 and 4 h post-LPS stimulation, we specifically focused on cluster F, which contained "stable responder" phosphosites upregulated by LPS at both the 1- and the 4-h time points. One of the most significantly enriched terms in this cluster was the GO term "cell junction." To identify proteins potentially responsible for the observed phenotype, we performed a functional protein network of the cluster F phosphoproteins belonging to this GO term by using STRING (Figure 5C; Table S4).[49] This analysis highlighted the most connected nodes (highest degree and network centrality). We focused on cofilin-1 (encoded by the *CFL1* gene, previously shown to regulate nuclear morphology both in interphase cells[50] and at the end of mitosis[51]), which was phosphorylated on serine 41 upon LPS treatment (Figures 5D–5F; Table S4). Phosphorylation of cofilin-1 at serine 41 has been previously observed in several phosphoproteomic studies, including in mouse dendritic cells and human cancer cells.[52–62] However, the functional relevance of this phosphorylation has not been previously studied.

We also verified the effect of LPS stimulation on lamin-A/C expression using our MS datasets. At both 1 and 4 h post-stimulation the total protein level of lamin-A/C (*LMNA* gene) was not reduced (Figures S5A–S5C). However, we did observe an increase in the phosphorylation of lamin-A/C at serine 12 (Figure S5D). It is possible, therefore, that the subtle reduction in lamin A/C levels observed following overnight LPS stimulation (Figures S3J and S3K) occurs over a longer time frame and may be influenced by serine 12 phosphorylation.

Intriguingly, our GO analysis also presented "release of cytochrome *c* from the mitochondria" as a major upregulated term. This is a major event in the apoptotic cascade and would suggest that LPS stimulation drives programmed cell death.[63] We therefore checked this using flow cytometry (Figure S5E). This revealed a small, but non-significant, increase in cell death in response to LPS stimulation following overnight LPS stimulation as previously observed.[64]

To determine whether cofilin-1^{pS41} drives nuclear deformation, we overexpressed GFP-tagged wild-type (WT) cofilin-1, along with phosphomimetic (S41E) and phospho-dead (S41A) cofilin-1 mutants, in moDCs. For the microscopy, we selected cells with comparable expression levels of the cofilin-1 variants based on the intensities of the GFP fluorescence. Analysis of the z-projected sizes of the nuclei revealed that both the phosphomimetic (S41E) and the phospho-dead (S41A) cofilin-1 mutants can induce a subtle deformation of the moDC nuclei (Figures 6A and 6B). We also verified that cofilin-1 S41E and S41A were not altering the shape of the nucleus by reducing moDC spreading. Indeed, although the nuclei were reduced in z-projected size, the z-projected size of the entire cell was not reduced (Figure S6A). Therefore, is seems likely that cofilin-1^{pS41} contributes to nuclear deformation but not to the de-spreading process.

It is surprising that both the phosphomimetic and the phospho-dead mutants could induce subtle deformation of the moDC nucleus in the x-y plane given the differing biochemical properties of glutamic acid and alanine. The reasons for this are unclear; however, phosphorylation can reprogram protein function[65] by altering protein shape and/or rewiring a protein's interactome.[66] Therefore we performed molecular simulations with enhanced sampling techniques, which indicated that the structure of cofilin-1 is very stable; phosphorylation of serine 41 (and dephosphorylation of serine 3) leaves the structure relatively unchanged (Figures S6B, S6C, and S6D). Therefore, our data suggest that phosphorylation of cofilin-1 at serine 41 may instead alter cofilin-1's interactome through loss of the OH group on the serine (as opposed to altering cofilin-1's molecular structure). We speculate that this will ultimately rewire the interactome of cofilin. However, confirming this will require further experimentation.

To further understand the contribution of cofilin^{pS41} to the deformation of the cell nucleus, we analyzed moDCs overexpressing WT or S41E cofilin-1, using Airyscan microscopy. First, we verified that the nuclei were deforming and not shrinking (Figures 6C and 6D), as we observed for activated moDCs (Figures 1B and 1C). This revealed that, although S41E cofilin-1 can significantly reduce the z-projected size, it does not significantly change the nuclear volume; the nuclei extend into the z plane, similar to our observations with LPS activation. Furthermore, qualitative observation of cofilin-1 S41E (as well as qualitative observation of S41A expressing moDCs) suggests

Figure 5. Phosphoproteomic analysis of dendritic cell inflammatory activation

(A) Hierarchical clustering analysis using Pearson correlation distance of phosphosite intensities. Values were normalized, imputed, batch-corrected, and scaled (*Z* score) before clustering. Only sites with one-way ANOVA FDR < 0.01 and functional score >0.45 were used for clustering. n = 6 donors.

(B) Gene ontology (GO) and pathway (KEGG and Reactome) enrichment analysis on each cluster shown in (A). Enrichment was performed on the phosphoprotein level against the entire proteome quantified.

(C) Functional STRING protein network of the phosphoproteins belonging to cluster F and to the GO "cell junction".

(D) Boxplot of the normalized MS signal, after log2 transformation, for the protein cofilin-1 (left) and the phosphorylated serine 41 of cofilin-1 (right). The p values were calculated by two-tailed paired Student's t test.

(E) MS/MS spectra for the cofilin-1 phosphopeptide containing the phosphorylated serine 41.

(F) Extracted MS2 ion chromatogram for the cofilin-1 phosphopeptide shown in (E). Each line represents a fragment ion. iRT, independent retention time (in minutes). Data information: for box-and-whisker plots, box represents 25th to 75th percentile, whiskers (when displayed) represent maximum and minimum values, and middle band represents data median.

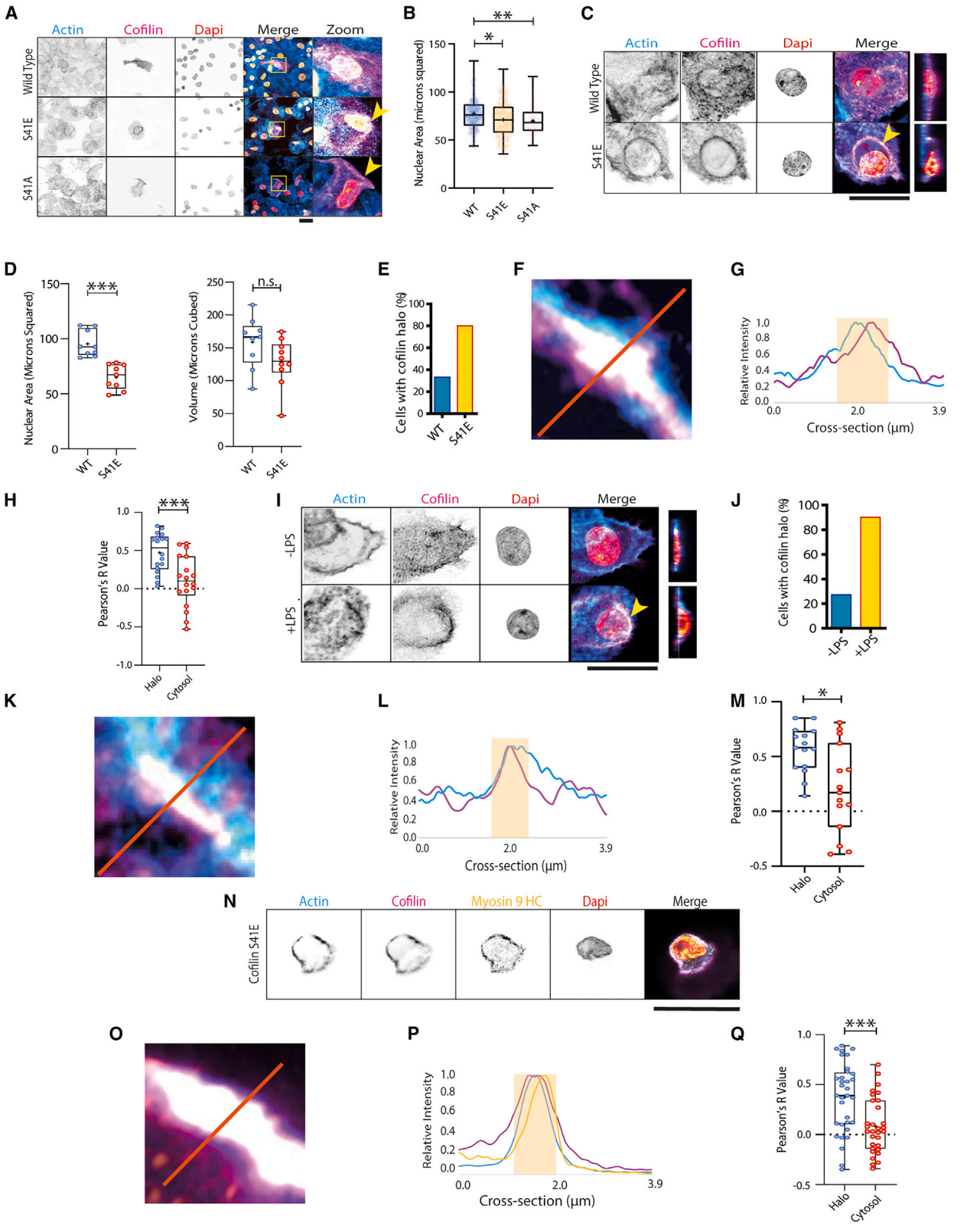

(legend on next page)

that it (and therefore cofilin-1^{pS41}) accumulates around the nucleus (Figure 6A). Therefore, we examined the nature of these structures using Airyscan microscopy. The majority of observed cells overexpressing cofilin-1 S41E form a cofilin-1 halo, in contrast to WT cofilin (Figures 6C and 6E). The majority of these halos co-localized with F-actin (Figures 6F–6H). We also noticed that F-actin filaments are lost from the nuclei in moDCs expressing both WT and S41E cofilin. These are likely lost as an overexpression artifact. We also determined the minimum and maximum distances between the halos and the nuclei (Figures S6E and S6F). This revealed that part of the halos are always juxtaposed to the nucleus, while other parts can be up to 5 μm away. Therefore it seems possible that any force transmission from the halos to the nuclei may be both direct and via cytoplasmic squeezing.

We also examined the impact of cofilin-1 S3 phosphorylation on z-projected nuclear size. Based on previous findings,[67] cofilin-1^{pS3} is dephosphorylated upon LPS stimulation, which has been reported to regulate nuclear morphology.[51] Dephosphorylation at this residue enables its actin-severing activity.[68] However, at both 1 and 4 h, this was a non-significant change in our phosphoproteomic data (Figure S4E). Furthermore, overexpression of a cofilin-1 S3A mutant (phospho-dead) was not sufficient to induce the nuclear membrane deformation in moDCs (Figures S7A and S7B).[69]

Using the mN2G-TS FRET probe, we confirmed that there is no difference in force across actin-based LINC complexes in cells expressing WT or S41E cofilin (Figures S7C and S7D). Therefore, S41E cofilin is able to remodel the nuclei through a mechanism that does not involve actin-based LINC complex remodeling. It seems possible that the observed cofilin halos are not passively sequestering actin away from the nucleus, but may instead be driving an active remodeling process. Indeed, Airyscan microscopy of endogenous cofilin-1 confirmed that a similar halo forms in the majority of LPS-stimulated cells (Figures 6I and 6J). We were able to observe co-localization between cofilin-1 and F-actin in approximately 50% of imaged activated cells (Figures 6K–6M). We therefore hypothesized that these halos may be contractile, and therefore, we stained for myosin 9 heavy chain in cells expressing mCherry-cofilin S41E. This revealed a strong co-localization between cofilin S41E and myosin motors (Figures 6N–6Q). We have therefore termed these halos CAM rings.

To test the impact of cofilin S41 phosphorylation on nuclear dynamics and migration, we first analyzed the impact of overexpressing WT or S41E cofilin on nuclear shape fluctuations (Figures 7A–7D; Videos S5 and S6). Consistent with LPS-stimulated moDC nuclei, we observed more nuclear fluctuations with our phosphomimetic mutant.

To test the impact of cofilin phosphorylation at serine 41 on 3D migration, we overexpressed mCitrine-WT and mCherry-S41E cofilin in activated moDCs, mixed the populations, and seeded them into bovine dermal-based collagen gels (concentration of 1.7 mg ml^{-1} as used above; Figures 7E–7I; Videos S7 and S8). This revealed that overexpression of cofilin-S41E increased the MSD in active moDCs (Figures 7J and 7K). While the increase in MSD was consistent for all donors assessed with a minimum increase of about 25% observed, the results were again variable

Figure 6. Nuclear deformation is driven by cofilin-1 S41 phosphorylation

(A) Confocal micrographs of dendritic cells expressing WT, S41E, or S41A cofilin-1 fused to GFP. Yellow arrowheads indicate qualitatively observed perinuclear cofilin-1 halos. Scale bar, 20 μm.

(B) Quantification of the z-projected nuclear area of dendritic cells expressing cofilin-1 variants (data points represent individual cells pooled from three donors; data are for at least 108 measurements per condition; statistics for individual donors are in Table S5).

(C) Airyscan images of dendritic cells expressing WT or S41E cofilin-1 variants. Yellow arrowhead indicates perinuclear cofilin-1 halo. Scale bar, 20 μm.

(D) z-projected area along with volume of the same nuclei of cells expressing either WT cofilin-1 or S41E cofilin-1 (data points represent individual cells pooled from three donors).

(E) Quantification of the cells with a cofilin-1 halo around the nucleus (expressing WT or S41E cofilin-1 observed in Airyscan images; minimum of nine cells per condition and three donors).

(F) Example of cofilin-1-F-actin co-localization in a dendritic cell expressing cofilin-1 S41E. Orange line, 3.9 μm.

(G) Line profile of normalized cofilin-1 (purple) and F-actin (blue) intensity as indicated in (F). Highlighted region indicates area of substantial overlap.

(H) Pearson's correlation coefficient of cofilin-1-F-actin at the halos and in the cytosol of cells expressing cofilin-1 S41E (data points represent individual cells pooled from three donors, minimum of 18 measurements per condition; three regions per compartment per cell were analyzed).

(I) Airyscan images of cofilin-1 and F-actin in dendritic cells cultured overnight in the presence or absence of LPS (overnight stimulation). Yellow arrowhead indicates perinuclear cofilin-1 halo. Scale bar, 20 μm.

(J) Quantification of the percentage of cells with a cofilin-1 halo around the nucleus (cultured in the presence or absence of LPS), observed in Airyscan images (minimum of 10 cells per condition and three donors).

(K) Example of cofilin-1-F-actin co-localization in dendritic cells cultured overnight with LPS.

(L) Line profile of normalized cofilin-1 (purple) and F-actin (blue) intensity as indicated in (K). Highlighted region indicates area of substantial overlap. Orange line, 3.9 μm.

(M) Pearson's correlation coefficient of cofilin-1-F-actin at the halos and in the cytosol of cells cultured overnight with LPS that displayed F-actin-cofilin-1 bundling (data points represent individual cells pooled from three donors, minimum of 15 measurements per condition).

(N) Airyscan images of dendritic cells with S41E cofilin-1 stained for F-actin and myosin 9 heavy chain (HC). Scale bar, 20 μm.

(O) Example of S41E cofilin-1-F-actin-myosin co-localization in a dendritic cell expressing cofilin-1 S41E. Orange line, 3.9 μm.

(P) Line profile of normalized cofilin-1 (purple), F-actin (blue), and myosin 9 HC (yellow) intensity as indicated in (O). Highlighted region indicates area of substantial overlap.

(Q) Pearson's correlation coefficient of cofilin-1-myosin 9 HC at the halos and in the cytosol of cells expressing cofilin-1 S41E (data points represent individual cells pooled from three donors, minimum of 31 measurements per condition). Statistical significance was calculated using two-tailed unpaired t tests for two-condition experiments or ANOVA/Tukey's multiple comparisons test for experiments with three or more conditions (with test selected according to distribution pattern of the data). A two-tailed paired t test was used for (H), (M), and (Q). *$p < 0.05$; **$p < 0.01$; ***$p < 0.001$. Error bars, SEM.

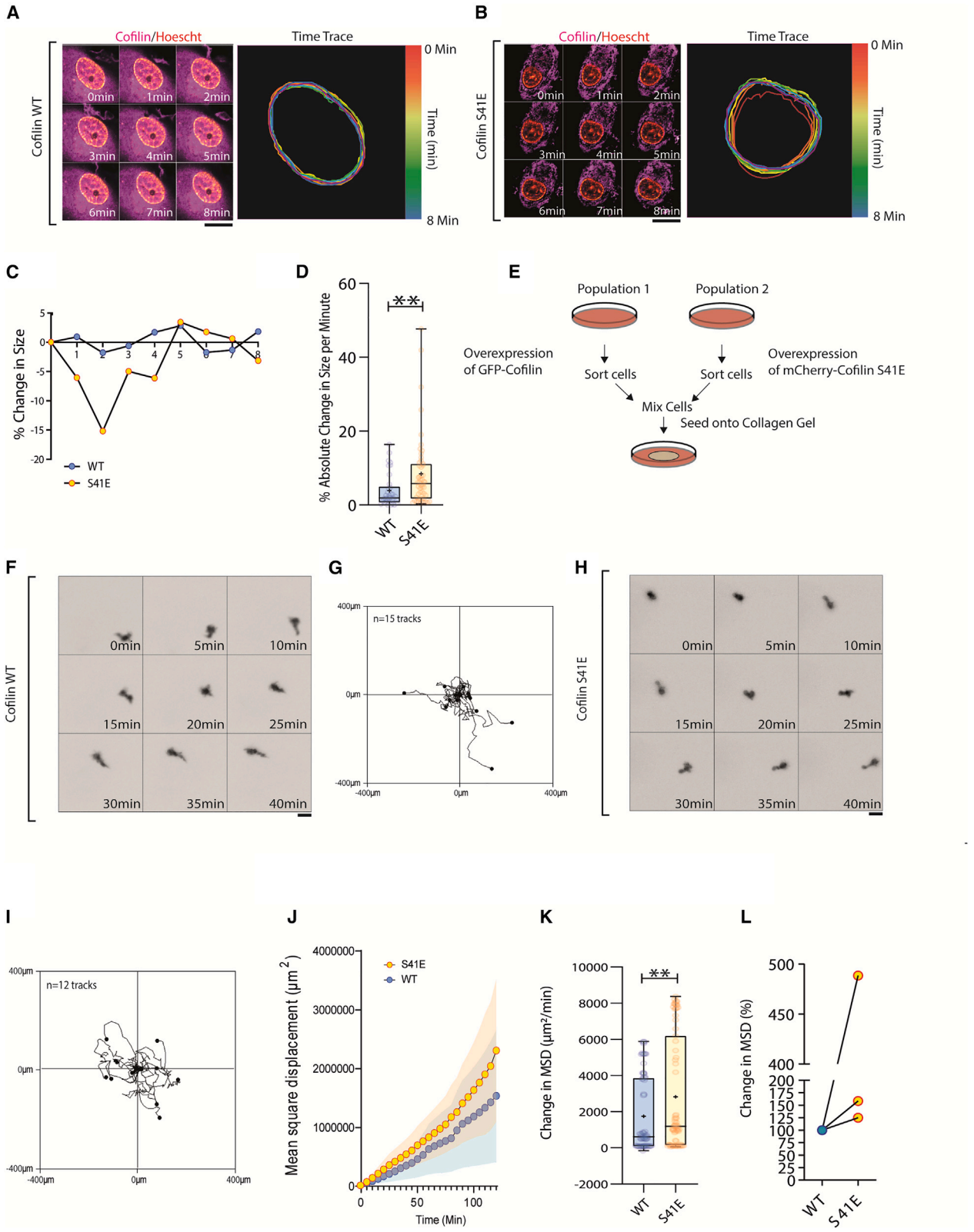

(legend on next page)

between donors (Figure 7L). We also stained for cofilin in moDCs migrating through collagen produced at 1.7 mg mL^{-1}. Although the density prevented consistent staining for a comparison between inactive and active moDCs, we did observe cofilin around the nucleus in active moDCs migrating in 3D (Figure S7E). Furthermore, we observed a decrease in the nuclear width-to-length ratio when comparing cells that presented a halo (Figure S7F) with those without, indicating that cofilin halos drive nuclear squeezing.

These results suggest that phosphorylation of cofilin at serine 41 mimics the increase in morphological dynamism associated with moDC activation, reducing the relative confinement exerted on moDCs by the ECM. As these collagen gels have holes approaching the physical limit of migration, we conclude that cofilin^{pS41}-driven nuclear remodeling facilitates efficient moDC migration through the ECM, likely through CAM-ring-mediated contractility.

DISCUSSION

Dendritic cells are found in virtually all tissues, yet they need to migrate to lymph nodes to initiate a novel adaptive immune response.[1] Therefore, dendritic cells must have extremely plastic biochemical and mechanosensitive signaling machinery that can adapt to residency within each tissue, yet override mechanical signals once activated. Indeed, activated dendritic cells are less adhesive,[5,22] and integrin-free dendritic cell migration is both viable and efficient.[20,21] However, a perceived disadvantage of adhesion-free migration is that the nucleus blocks migration through small pores (<3 μm) that could otherwise be expanded through ECM remodeling.[31] Our study suggests that dendritic cell activation can (partially) compensate for this, as the nucleus becomes more spherically deformed and is better able to pass through 2-μm gaps in the ECM. These changes to the shape of the nucleus seem to also be partially passive, via a reduction in adhesion, and partially active, with cofilin^{pS41} promoting the assembly of perinuclear CAM rings. Indeed, the assembly of a contractile ring around the nucleus in response to LPS stimulation makes sense of the fact that the dendritic nucleus seems to be able to better pass through gaps in the ECM without becoming consistently softer (indeed, it may be stiffening in response to LPS stimulation).

Dendritic cell activation is extremely well understood at the genetic level, with numerous signaling receptors and transcription factors identified.[70] However, the complex (de)phosphorylation events underpinning this activation are poorly understood. Although a few high-quality phosphoproteomic studies describing these (de)phosphorylation events in dendritic cells have been produced,[61,71,72] only one study has been published for human dendritic cells.[72] Our phosphoproteomic data both contribute to this understanding and provide (to date) the most comprehensive phosphoproteomic description of human myeloid cell activation, having identified 2,068 statically significant (de)phosphorylation events, including an adhesion-associated signaling cluster, focused around cofilin-1^{pS41}.

How does cofilin-1^{pS41} drive migration through the ECM? Our data suggest that this might be ultimately achieved through force transmission to the nucleus, via perinuclear CAM rings. Indeed, previous work has shown that dendritic cells find paths through the ECM by pushing their nucleus into multiple pores in their immediate vicinity.[23] This allows the dendritic cell to select the largest pore to migrate through. Although our data do not demonstrate that myosin is actively contracting at these rings, this model is consistent with findings that dendritic cell activation is accompanied by increased myosin-based squeezing of the nucleus through ECM gaps.[47] It is also worth noting that the increase in MSD across multiple donors in 3D ECM was far larger as a percentage than the change in nuclear size in 2D (~25% MSD increase compared with an ~9% reduction in z-projected nuclear size). However, this is consistent with cofilin s41 phosphorylation playing a critical role in 3D migration that is not conserved to 2D; in 2D there are no pores for the nucleus to be squeezed through (although our 2D experiments have enabled us to make predictions regarding 3D migration). Indeed, many studies have shown that 2D- and 3D-migration modes are very different. For instance, the disruption of microtubules (via nocodazole treatment) in dendritic cells in 2D has relatively little effect on migration efficiency, but leads to cellular fragmentation in 3D.[23] This is due to the dendritic cell's inability to correctly position and reposition its nucleus, which is critical for dendritic cell

Figure 7. S41 phosphorylation of cofilin increases migration in confined environments

(A) Airyscan movie and time trace of nucleus in dendritic cell overexpressing WT cofilin. Scale bar, 10 μm.
(B) Airyscan movie and time trace of nucleus in dendritic cell overexpressing cofilin S41E. Scale bar, 10 μm.
(C) Example traces of nuclear size fluctuations for dendritic cells overexpressing WT cofilin (blue) or cofilin S41E (yellow).
(D) Quantification of absolute percentage changes in nuclear size over time (data points represent individual cells pooled from three donors, minimum of 67 measurements per condition).
(E) Schematic demonstrating migration experiment setup.
(F) Stills from representative time-lapse microscopy of activated dendritic cell overexpressing WT cofilin. Scale bar, 20 μm.
(G) Example migration traces of activated dendritic cell overexpressing WT cofilin.
(H) Stills from representative time-lapse microscopy of activated dendritic cell overexpressing S41E cofilin. Scale bar, 20 μm.
(I) Example migration traces of activated dendritic cell overexpressing S41E cofilin.
(J) Example mean square displacement (MSD) of activated dendritic cells overexpressing WT or S41E cofilin. Shaded region represents SEM.
(K) Quantification of rate of MSD change for activated dendritic cells overexpressing WT or S41E cofilin (data points represent individual cells pooled from three donors, 75 measurements per condition; statistics for individual donors are in Table S5).
(L) Donor breakdown of the rate of MSD change per donor, expressed as a percentage change from cofilin WT to cofilin S41E. Data points show donor averages.
Data information: statistical significance was calculated using two-tailed unpaired t tests (with test selected according to distribution pattern of the data). **$p < 0.01$. Error bars, SEM. For box-and-whisker plots, box represents 25th to 75th percentile, whiskers represent maximum and minimum values, middle band represents data median, and + represents data mean.

pathfinding in 3D.[23] It is also unclear how long CAM rings would persist during long-range 3D migration. Actin-based retraction fibers are thought to be dynamically assembled in response to cues from the ECM, followed by disassembly.[73] Presumably, CAM rings follow the same pattern. In conclusion, our data suggest that dendritic cell activation triggers nuclear deformation via a reduction in cell-matrix adhesion and drives enhanced transmigration of the nucleus through small ($\leq$2-μm) gaps in the ECM.

Limitations of the study

Dendritic cell migration is a highly studied process, yet understanding human dendritic cell migration has many challenges. For instance, interpreting experimental variability is difficult, as primary moDCs are a heterogeneous cell population, and cells from different donors present varying responses to LPS stimulation.[74] Furthermore, many of our experiments utilized overnight LPS stimulation (in the range of 18–24 h of LPS stimulation). While this is standard practice for studies of dendritic cells, most large datasets derived from dendritic cells utilize very small time windows following LPS stimulation, because human myeloid cells are non-proliferative, limiting the amount of material available per experiment.

It is also unclear why cofilin S41E produces a phenotype similar to that of cofilin S41A, in terms of a subtle nuclear shape changer. While the addition of a negatively charged phosphate group has long been known to enable new protein-protein interactions,[75] the breaking of hydrogen bonds through the addition of a phosphate group (removing the hydrogen from an OH group), although theoretically possible, has not been definitively proven.

Finally, the use of primary cells also hampers the utilization of many established techniques that can be used with cell lines. For instance, we cannot suppress the expression of endogenous cofilin prior to overexpressing our recombinant variants. This has hampered our ability to differentiate the effects of cofilin phosphorylation at serine 41 at the nucleus compared with other subcellular actin structures. Thus, a more extensive analysis of the effect of cofilin phosphorylation on dendritic cell migration will require alternative systems, such as mouse models.

STAR★METHODS

Detailed methods are provided in the online version of this paper and include the following:

- KEY RESOURCES TABLE
- RESOURCE AVAILABILITY
  - Lead contact
  - Materials availability
  - Data and code availability
- EXPERIMENTAL MODEL AND STUDY PARTICIPANT DETAILS
- METHOD DETAILS
  - Reagents antibodies
  - Total cell lysis and western blotting
  - Confocal microscopy
  - ECM coating of glass coverslips
  - Inhibitors
  - Bodipy-C10
  - Atomic force microscopy
- FLOW CYTOMETRY
  - Plasmids
  - Ratiometric FRET analysis
  - 3D cell culture
  - Micropatterned substrate
  - Gelatin impregnated filters
  - Cell lysis and digestion for proteomics analysis
  - Enrichment of phosphorylated peptides
  - Liquid chromatography-tandem mass spectrometry
  - Mass spectrometry raw data processing
  - Bioinformatic analysis
  - Proteome data
  - Phosphoproteome data
  - Molecular modeling: General simulation details
  - Molecular modeling: All-atom replica exchange MD
  - Time-lapse microscopy
- QUANTIFICATION AND STATISTICAL ANALYSIS

SUPPLEMENTAL INFORMATION

Supplemental information can be found online at https://doi.org/10.1016/j.celrep.2024.113866.

ACKNOWLEDGMENTS

We are thankful to P. Grijpstra for technical support throughout the project. We are also grateful to F. Stempels for advice regarding FLIM observations. G.v.d. Bogaart is supported by the European Research Council (ERC) under the European Union's Horizon 2020 research innovation program (grant agreement 862137) and ZonMw (project grant 09120011910001). The proteomics experiments performed in this project and G.F.'s salary were funded by the European Union's Horizon 2020 research and innovation program under grant agreement EPIC-XS-823839. Work at the NNF CPR is funded by a donation from the NNF (NNF14CC0001). C.K. is funded by the European Union's Horizon 2020 research and innovation program under the Marie Sklodowska-Curie grant agreement 861389. L.Q.C. is supported by grant 11618 from the Dutch Cancer Society. W.H.R. is supported by a FOM projectruimte grant.

AUTHOR CONTRIBUTIONS

H.W. and G.v.d. Bogaart designed the project and wrote the manuscript. H.W. performed the majority of the experiments. G.F., C.K., and J.V.O. planned, carried out, and analyzed the proteomic and phosphoproteomic experiments. G.v.d. Borg and W.H.R. planned, carried out, and analyzed the AFM experiments. L.Q.C. and R.C. carried out 3D collagen migration assays. N.v.H. and H.J.R. planned, carried out, and analyzed molecular modeling experiments. B.C., F.F., R.d.B., S. Maassen., M.V.B., S. Mahajan, D.D., and F.B.. carried out experiments.

DECLARATION OF INTERESTS

The authors declare no competing interests.

Received: January 19, 2023
Revised: October 13, 2023
Accepted: February 8, 2024
Published: February 27, 2024

REFERENCES

1. Patente, T.A., Pinho, M.P., Oliveira, A.A., Evangelista, G.C.M., Bergami-Santos, P.C., and Barbuto, J.A.M. (2018). Human Dendritic Cells: Their

Heterogeneity and Clinical Application Potential in Cancer Immunotherapy. Front. Immunol. *9*, 3176. https://doi.org/10.3389/FIMMU.2018.03176.

2. Park, S., Matte-Martone, C., Gonzalez, D.G., Lathrop, E.A., May, D.P., Pineda, C.M., Moore, J.L., Boucher, J.D., Marsh, E., Schmitter-Sánchez, A., et al. (2021). Skin-resident immune cells actively coordinate their distribution with epidermal cells during homeostasis. Nat. Cell Biol. *23*, 476–484. https://doi.org/10.1038/s41556-021-00670-5.

3. Chakraborty, M., Chu, K., Shrestha, A., Revelo, X.S., Zhang, X., Gold, M.J., Khan, S., Lee, M., Huang, C., Akbari, M., et al. (2021). Mechanical Stiffness Controls Dendritic Cell Metabolism and Function. Cell Rep. *34*, 108609. https://doi.org/10.1016/J.CELREP.2020.108609.

4. Meddens, M.B.M., Pandzic, E., Slotman, J.A., Guillet, D., Joosten, B., Mennens, S., Paardekooper, L.M., Houtsmuller, A.B., Van Den Dries, K., Wiseman, P.W., and Cambi, A. (2016). Actomyosin-dependent dynamic spatial patterns of cytoskeletal components drive mesoscale podosome organization. Nat. Commun. *7*, 13127. https://doi.org/10.1038/ncomms13127.

5. West, M.A., Prescott, A.R., Chan, K.M., Zhou, Z., Rose-John, S., Scheller, J., and Watts, C. (2008). TLR ligand–induced podosome disassembly in dendritic cells is ADAM17 dependent. J. Cell Biol. *182*, 993–1005. https://doi.org/10.1083/JCB.200801022.

6. Acton, S.E., Farrugia, A.J., Astarita, J.L., Mourão-Sá, D., Jenkins, R.P., Nye, E., Hooper, S., van Blijswijk, J., Rogers, N.C., Snelgrove, K.J., et al. (2014). Dendritic cells control fibroblastic reticular network tension and lymph node expansion. Nature *514*, 498–502. https://doi.org/10.1038/nature13814.

7. Martinez, V.G., Pankova, V., Krasny, L., Singh, T., Makris, S., White, I.J., Benjamin, A.C., Dertschnig, S., Horsnell, H.L., Kriston-Vizi, J., et al. (2019). Fibroblastic Reticular Cells Control Conduit Matrix Deposition during Lymph Node Expansion. Cell Rep. *29*, 2810–2822.e5. https://doi.org/10.1016/j.celrep.2019.10.103.

8. Assen, F.P., Abe, J., Hons, M., Hauschild, R., Shamipour, S., Kaufmann, W.A., Costanzo, T., Krens, G., Brown, M., Ludewig, B., et al. (2022). Multitier mechanics control stromal adaptations in the swelling lymph node. Nat. Immunol. *23*, 1246–1255. https://doi.org/10.1038/S41590-022-01257-4.

9. Hynes, R.O. (2012). Evolution: The evolution of metazoan extracellular matrix. J. Cell Biol. *196*, 671–679. https://doi.org/10.1083/JCB.201109041.

10. McBeath, R., Pirone, D.M., Nelson, C.M., Bhadriraju, K., and Chen, C.S. (2004). Cell Shape, Cytoskeletal Tension, and RhoA Regulate Stem Cell Lineage Commitment. Dev. Cell *6*, 483–495. https://doi.org/10.1016/S1534-5807(04)00075-9.

11. Connelly, J.T., Gautrot, J.E., Trappmann, B., Tan, D.W.M., Donati, G., Huck, W.T.S., and Watt, F.M. (2010). Actin and serum response factor transduce physical cues from the microenvironment to regulate epidermal stem cell fate decisions. Nat. Cell Biol. *12*, 711–718. https://doi.org/10.1038/NCB2074.

12. Murray, P., Prewitz, M., Hopp, I., Wells, N., Zhang, H., Cooper, A., Parry, K.L., Short, R., Antoine, D.J., and Edgar, D. (2013). The self-renewal of mouse embryonic stem cells is regulated by cell–substratum adhesion and cell spreading. Int. J. Biochem. Cell Biol. *45*, 2698–2705. https://doi.org/10.1016/J.BIOCEL.2013.07.001.

13. Carley, E., Stewart, R.M., Zieman, A., Jalilian, I., King, D.E., Zubek, A., Lin, S., Horsley, V., and King, M.C. (2021). The linc complex transmits integrin-dependent tension to the nuclear lamina and represses epidermal differentiation. Elife *10*, e58541. https://doi.org/10.7554/ELIFE.58541.

14. De Belly, H., Stubb, A., Yanagida, A., Labouesse, C., Jones, P.H., Paluch, E.K., and Chalut, K.J. (2021). Membrane Tension Gates ERK-Mediated Regulation of Pluripotent Cell Fate. Stem Cell. *28*, 273–284.e6. https://doi.org/10.1016/j.stem.2020.10.018.

15. Maniotis, A.J., Chen, C.S., and Ingber, D.E. (1997). Demonstration of mechanical connections between integrins, cytoskeletal filaments, and nucleoplasm that stabilize nuclear structure. Proc. Natl. Acad. Sci. USA *94*, 849–854. https://doi.org/10.1073/PNAS.94.3.849.

16. Khatau, S.B., Hale, C.M., Stewart-Hutchinson, P.J., Patel, M.S., Stewart, C.L., Searson, P.C., Hodzic, D., and Wirtz, D. (2009). A perinuclear actin cap regulates nuclear shape. Proc. Natl. Acad. Sci. *106*, 19017–19022. https://doi.org/10.1073/PNAS.0908686106.

17. Lovett, D.B., Shekhar, N., Nickerson, J.A., Roux, K.J., and Lele, T.P. (2013). Modulation of Nuclear Shape by Substrate Rigidity. Cell. Mol. Bioeng. *6*, 230–238. https://doi.org/10.1007/S12195-013-0270-2.

18. Vishavkarma, R., Raghavan, S., Kuyyamudi, C., Majumder, A., Dhawan, J., and Pullarkat, P.A. (2014). Role of Actin Filaments in Correlating Nuclear Shape and Cell Spreading. PLoS One *9*, e107895. https://doi.org/10.1371/JOURNAL.PONE.0107895.

19. Chen, B., Co, C., and Ho, C.C. (2015). Cell Shape Dependent Regulation of Nuclear Morphology. Biomaterials *67*, 129–136. https://doi.org/10.1016/J.BIOMATERIALS.2015.07.017.

20. Lämmermann, T., Bader, B.L., Monkley, S.J., Worbs, T., Wedlich-Söldner, R., Hirsch, K., Keller, M., Förster, R., Critchley, D.R., Fässler, R., and Sixt, M. (2008). Rapid leukocyte migration by integrin-independent flowing and squeezing. Nature *453*, 51–55. https://doi.org/10.1038/nature06887.

21. Reversat, A., Gaertner, F., Merrin, J., Stopp, J., Tasciyan, S., Aguilera, J., De Vries, I., Hauschild, R., Hons, M., Piel, M., et al. (2020). Cellular locomotion using environmental topography. Nature *582*, 582–585. https://doi.org/10.1038/s41586-020-2283-z.

22. van Helden, S.F.G., Krooshoop, D.J.E.B., Broers, K.C.M., Raymakers, R.A.P., Figdor, C.G., van Leeuwen, F.N., and Krooshoop, D.J.E.B. (2006). A Critical Role for Prostaglandin E2 in Podosome Dissolution and Induction of High-Speed Migration during Dendritic Cell Maturation. J. Immunol. *177*, 1567–1574. https://doi.org/10.4049/JIMMUNOL.177.3.1567.

23. Renkawitz, J., Kopf, A., Stopp, J., de Vries, I., Driscoll, M.K., Merrin, J., Hauschild, R., Welf, E.S., Danuser, G., Fiolka, R., and Sixt, M. (2019). Nuclear positioning facilitates amoeboid migration along the path of least resistance. Nature *568*, 546–550. https://doi.org/10.1038/S41586-019-1087-5.

24. Lomakin, A.J., Cattin, C.J., Cuvelier, D., Alraies, Z., Molina, M., Nader, G.P.F., Srivastava, N., Sáez, P.J., Garcia-Arcos, J.M., Zhitnyak, I.Y., et al. (2020). The nucleus acts as a ruler tailoring cell responses to spatial constraints. Science *370*, eaba2894. https://doi.org/10.1126/SCIENCE.ABA2894.

25. Venturini, V., Pezzano, F., Castro, F.C., Häkkinen, H.M., Jiménez-Delgado, S., Colomer-Rosell, M., Marro, M., Tolosa-Ramon, Q., Paz-López, S., Valverde, M.A., et al. (2020). The nucleus measures shape changes for cellular proprioception to control dynamic cell behavior. Science *370*, eaba2644. https://doi.org/10.1126/SCIENCE.ABA2644.

26. Petrie, R.J., Koo, H., and Yamada, K.M. (2014). Generation of compartmentalized pressure by a nuclear piston governs cell motility in a 3D matrix. Science *345*, 1062–1065. https://doi.org/10.1126/science.1256965.

27. Gilbert, H.T.J., Mallikarjun, V., Dobre, O., Jackson, M.R., Pedley, R., Gilmore, A.P., Richardson, S.M., and Swift, J. (2019). Nuclear decoupling is part of a rapid protein-level cellular response to high-intensity mechanical loading. Nat. Commun. *10*, 4149. https://doi.org/10.1038/s41467-019-11923-1.

28. Davidson, P.M., Battistella, A., Déjardin, T., Betz, T., Plastino, J., Borghi, N., Cadot, B., and Sykes, C. (2020). Nesprin-2 accumulates at the front of the nucleus during confined cell migration. EMBO Rep. *21*, e49910. https://doi.org/10.15252/EMBR.201949910.

29. Nava, M.M., Miroshnikova, Y.A., Biggs, L.C., Whitefield, D.B., Metge, F., Boucas, J., Vihinen, H., Jokitalo, E., Li, X., García Arcos, J.M., et al. (2020). Heterochromatin-Driven Nuclear Softening Protects the Genome against Mechanical Stress-Induced Damage. Cell *181*, 800–817.e22. https://doi.org/10.1016/J.CELL.2020.03.052.

30. Newman, D., Young, L.E., Waring, T., Brown, L., Wolanska, K.I., MacDonald, E., Charles-Orszag, A., Goult, B.T., Caswell, P.T., Sakuma, T., et al. (2023). 3D matrix adhesion feedback controls nuclear force coupling to drive invasive cell migration Actomyosin force engagement displaces Git-bPix-Myo18A, establishing a feedback loop 3D matrix adhesion feedback controls nuclear force coupling to drive invasive cell migration. Cell Rep. *42*, 113554. https://doi.org/10.1016/j.celrep.2023.113554.

31. Wolf, K., te Lindert, M., Krause, M., Alexander, S., te Riet, J., Willis, A.L., Hoffman, R.M., Figdor, C.G., Weiss, S.J., and Friedl, P. (2013). Physical limits of cell migration: Control by ECM space and nuclear deformation and tuning by proteolysis and traction force. J. Cell Biol. *201*, 1069–1084. https://doi.org/10.1083/JCB.201210152.

32. Baranov, M., Ter Beest, M., Reinieren-Beeren, I., Cambi, A., Figdor, C.G., and van den Bogaart, G. (2014). Podosomes of dendritic cells facilitate antigen sampling. J. Cell Sci. *127*, 1052–1064. https://doi.org/10.1242/JCS.141226.

33. Thiam, H.-R., Vargas, P., Carpi, N., Crespo, C.L., Raab, M., Terriac, E., King, M.C., Jacobelli, J., Alberts, A.S., Stradal, T., et al. (2016). Perinuclear Arp2/3-driven actin polymerization enables nuclear deformation to facilitate cell migration through complex environments. Nat. Commun. *7*, 10997. https://doi.org/10.1038/ncomms10997.

34. Arsenovic, P.T., and Conway, D.E. (2018). Using Nesprin Tension Sensors to Measure Force on the LINC Complex. Methods Mol. Biol. *1840*, 59–71. https://doi.org/10.1007/978-1-4939-8691-0_6.

35. Woroniuk, A., Porter, A., White, G., Newman, D.T., Diamantopoulou, Z., Waring, T., Rooney, C., Strathdee, D., Marston, D.J., Hahn, K.M., et al. (2018). STEF/TIAM2-mediated Rac1 activity at the nuclear envelope regulates the perinuclear actin cap. Nat. Commun. *9*, 2124. https://doi.org/10.1038/s41467-018-04404-4.

36. Gaertner, F., Reis-Rodrigues, P., de Vries, I., Hons, M., Aguilera, J., Riedl, M., Leithner, A., Tasciyan, S., Kopf, A., Merrin, J., et al. (2022). WASp triggers mechanosensitive actin patches to facilitate immune cell migration in dense tissues. Dev. Cell *57*, 47–62.e9. https://doi.org/10.1016/J.DEVCEL.2021.11.024.

37. Sutoh Yoneyama, M., Hatakeyama, S., Habuchi, T., Inoue, T., Nakamura, T., Funyu, T., Wiche, G., Ohyama, C., and Tsuboi, S. (2014). Vimentin intermediate filament and plectin provide a scaffold for invadopodia, facilitating cancer cell invasion and extravasation for metastasis. Eur. J. Cell Biol. *93*, 157–169. https://doi.org/10.1016/J.EJCB.2014.03.002.

38. Shaebani, M.R., Stankevicins, L., Vesperini, D., Urbanska, M., Flormann, D.A.D., Terriac, E., Gad, A.K.B., Cheng, F., Eriksson, J.E., and Lautenschl€ Ager, F. (2022). Effects of vimentin on the migration, search efficiency, and mechanical resilience of dendritic cells. Biophys. J. *121*, 3950–3961. https://doi.org/10.1016/j.bpj.2022.08.033.

39. Duarte, S., Viedma-Poyatos, Á., Navarro-Carrasco, E., Martínez, A.E., Pajares, M.A., and Pérez-Sala, D. (2019). Vimentin filaments interact with the actin cortex in mitosis allowing normal cell division. Nat. Commun. *10*, 4200. https://doi.org/10.1038/S41467-019-12029-4.

40. Serres, M.P., Samwer, M., Truong Quang, B.A., Lavoie, G., Perera, U., Görlich, D., Charras, G., Petronczki, M., Roux, P.P., and Paluch, E.K. (2020). F-Actin Interactome Reveals Vimentin as a Key Regulator of Actin Organization and Cell Mechanics in Mitosis. Dev. Cell *52*, 210–222.e7. https://doi.org/10.1016/J.DEVCEL.2019.12.011.

41. Swift, J., Ivanovska, I.L., Buxboim, A., Harada, T., Dingal, P.C.D.P., Pinter, J., Pajerowski, J.D., Spinler, K.R., Shin, J.-W., Tewari, M., et al. (2013). Nuclear Lamin-A Scales with Tissue Stiffness and Enhances Matrix-Directed Differentiation. Science *341*, 1240104. https://doi.org/10.1126/science.1240104.

42. Turan, A., Grosche, L., Krawczyk, A., Mühl-Zürbes, P., Drassner, C., Düthorn, A., Kummer, M., Hasenberg, M., Voortmann, S., Jastrow, H., et al. (2019). Autophagic degradation of lamins facilitates the nuclear egress of herpes simplex virus type 1. J. Cell Biol. *218*, 508–523. https://doi.org/10.1083/JCB.201801151.

43. Mika, J.T., Thompson, A.J., Dent, M.R., Brooks, N.J., Michiels, J., Hofkens, J., and Kuimova, M.K. (2016). Measuring the Viscosity of the Escherichia coli Plasma Membrane Using Molecular Rotors. Biophys. J. *111*, 1528–1540. https://doi.org/10.1016/J.BPJ.2016.08.020.

44. Piontek, M.C., and Roos, W.H. (2018). Atomic Force Microscopy: An Introduction. Methods Mol. Biol. *1665*, 243–258. https://doi.org/10.1007/978-1-4939-7271-5_13.

45. Blumenthal, D., Chandra, V., Avery, L., and Burkhardt, J.K. (2020). Mouse T cell priming is enhanced by maturation-dependent stiffening of the dendritic cell cortex. Elife *9*, e55995. https://doi.org/10.7554/ELIFE.55995.

46. Rigato, A., Rico, F., Eghiaian, F., Piel, M., and Scheuring, S. (2015). Atomic Force Microscopy Mechanical Mapping of Micropatterned Cells Shows Adhesion Geometry-Dependent Mechanical Response on Local and Global Scales. ACS Nano *9*, 5846–5856. https://doi.org/10.1021/ACSNANO.5B00430.

47. Barbier, L., Sáez, P.J., Attia, R., Lennon-Duménil, A.M., Lavi, I., Piel, M., and Vargas, P. (2019). Myosin II activity is selectively needed for migration in highly confined microenvironments in mature dendritic cells. Front. Immunol. *10*, 747. https://doi.org/10.3389/FIMMU.2019.00747/BIBTEX.

48. Franciosa, G., Martinez-Val, A., and Olsen, J.V. (2020). Deciphering the human phosphoproteome. Nat. Biotechnol. *38*, 285–286. https://doi.org/10.1038/S41587-020-0441-3.

49. Szklarczyk, D., Gable, A.L., Lyon, D., Junge, A., Wyder, S., Huerta-Cepas, J., Simonovic, M., Doncheva, N.T., Morris, J.H., Bork, P., et al. (2019). STRING v11: protein-protein association networks with increased coverage, supporting functional discovery in genome-wide experimental datasets. Nucleic Acids Res. *47*, D607–D613. https://doi.org/10.1093/NAR/GKY1131.

50. Wiggan, O., Schroder, B., Krapf, D., Bamburg, J.R., and Deluca, J.G. (2017). Cofilin Regulates Nuclear Architecture through a Myosin-II Dependent Mechanotransduction Module. Sci. Rep. *7*, 40953. https://doi.org/10.1038/SREP40953.

51. Baarlink, C., Plessner, M., Sherrard, A., Morita, K., Misu, S., Virant, D., Kleinschnitz, E.-M., Harniman, R., Alibhai, D., Baumeister, S., et al. (2017). A transient pool of nuclear F-actin at mitotic exit controls chromatin organization. Nat. Cell Biol. *19*, 1389–1399. https://doi.org/10.1038/ncb3641.

52. Dally, S., Bredoux, R., Corvazier, E., Andersen, J.P., Clausen, J.D., Dode, L., Fanchaouy, M., Gelebart, P., Monceau, V., Del Monte, F., et al. (2006). Ca^{2+} -ATPases in non-failing and failing heart: evidence for a novel cardiac sarco/endoplasmic reticulum Ca^{2+} -ATPase 2 isoform (SERCA2c). Biochem. J. *395*, 249–258. https://doi.org/10.1042/BJ20051427.

53. Kettenbach, A.N., Schweppe, D.K., Faherty, B.K., Pechenick, D., Pletnev, A.A., and Gerber, S.A. (2011). Quantitative phosphoproteomics identifies substrates and functional modules of Aurora and Polo-like kinase activities in mitotic cells. Sci. Signal. *4*, rs5. https://doi.org/10.1126/SCISIGNAL.2001497.

54. Klammer, M., Kaminski, M., Zedler, A., Oppermann, F., Blencke, S., Marx, S., Müller, S., Tebbe, A., Godl, K., and Schaab, C. (2012). Phosphosignature predicts dasatinib response in non-small cell lung cancer. Mol. Cell. Proteomics *11*, 651–668. https://doi.org/10.1074/MCP.M111.016410.

55. Zhou, H., Di Palma, S., Preisinger, C., Peng, M., Polat, A.N., Heck, A.J.R., and Mohammed, S. (2013). Toward a comprehensive characterization of a human cancer cell phosphoproteome. J. Proteome Res. *12*, 260–271. https://doi.org/10.1021/PR300630K.

56. Shiromizu, T., Adachi, J., Watanabe, S., Murakami, T., Kuga, T., Muraoka, S., and Tomonaga, T. (2013). Identification of missing proteins in the neXtProt database and unregistered phosphopeptides in the PhosphoSitePlus database as part of the Chromosome-centric Human Proteome Project. J. Proteome Res. *12*, 2414–2421. https://doi.org/10.1021/PR300825V.

57. Sharma, K., D'Souza, R.C.J., Tyanova, S., Schaab, C., Wiśniewski, J.R., Cox, J., and Mann, M. (2014). Ultradeep human phosphoproteome reveals a distinct regulatory nature of Tyr and Ser/Thr-based signaling. Cell Rep. *8*, 1583–1594. https://doi.org/10.1016/J.CELREP.2014.07.036.

58. Mertins, P., Qiao, J.W., Patel, J., Udeshi, N.D., Clauser, K.R., Mani, D.R., Burgess, M.W., Gillette, M.A., Jaffe, J.D., and Carr, S.A. (2013). Integrated proteomic analysis of post-translational modifications by serial enrichment. Nat. Methods *10*, 634–637. https://doi.org/10.1038/NMETH.2518.

59. Mertins, P., Yang, F., Liu, T., Mani, D.R., Petyuk, V.A., Gillette, M.A., Clauser, K.R., Qiao, J.W., Gritsenko, M.A., Moore, R.J., et al. (2014). Ischemia in tumors induces early and sustained phosphorylation changes in stress kinase pathways but does not affect global protein levels. Mol. Cell. Proteomics *13*, 1690–1704. https://doi.org/10.1074/MCP.M113.036392.

60. Mertins, P., Mani, D.R., Ruggles, K.V., Gillette, M.A., Clauser, K.R., Wang, P., Wang, X., Qiao, J.W., Cao, S., Petralia, F., et al. (2016). Proteogenomics connects somatic mutations to signalling in breast cancer. Nature *534*, 55–62. https://doi.org/10.1038/NATURE18003.

61. Mertins, P., Przybylski, D., Yosef, N., Qiao, J., Clauser, K., Raychowdhury, R., Eisenhaure, T.M., Maritzen, T., Haucke, V., Satoh, T., et al. (2017). An Integrative Framework Reveals Signaling-to-Transcription Events in Toll-like Receptor Signaling. Cell Rep. *19*, 2853–2866. https://doi.org/10.1016/J.CELREP.2017.06.016.

62. Dephoure, N., Zhou, C., Villén, J., Beausoleil, S.A., Bakalarski, C.E., Elledge, S.J., and Gygi, S.P. (2008). A quantitative atlas of mitotic phosphorylation. Proc. Natl. Acad. Sci. USA *105*, 10762–10767. https://doi.org/10.1073/PNAS.0805139105.

63. Singh, R., Letai, A., and Sarosiek, K. (2019). Regulation of apoptosis in health and disease: the balancing act of BCL-2 family proteins. Nat. Rev. Mol. Cell Biol. *20*, 175–193. https://doi.org/10.1038/s41580-018-0089-8.

64. Dingjan, I., Verboogen, D.R., Paardekooper, L.M., Revelo, N.H., Sittig, S.P., Visser, L.J., Mollard, G.F.v., Henriet, S.S., Figdor, C.G., Ter Beest, M., and van den Bogaart, G. (2016). Lipid peroxidation causes endosomal antigen release for cross-presentation. Sci. Rep. *6*, 22064. https://doi.org/10.1038/SREP22064.

65. Seok, S.H. (2021). Structural Insights into Protein Regulation by Phosphorylation and Substrate Recognition of Protein Kinases/Phosphatases. Life *11*, 957. https://doi.org/10.3390/LIFE11090957.

66. Pawson, T., and Scott, J.D. (2005). Protein phosphorylation in signaling–50 years and counting. Trends Biochem. Sci. *30*, 286–290. https://doi.org/10.1016/j.tibs.2005.04.013.

67. Verdijk, P., van Veelen, P.A., de Ru, A.H., Hensbergen, P.J., Mizuno, K., Koerten, H.K., Koning, F., Tensen, C.P., and Mommaas, A.M. (2004). Morphological changes during dendritic cell maturation correlate with cofilin activation and translocation to the cell membrane. Eur. J. Immunol. *34*, 156–164. https://doi.org/10.1002/EJI.200324241.

68. Bravo-Cordero, J.J., Magalhaes, M.A.O., Eddy, R.J., Hodgson, L., and Condeelis, J. (2013). Functions of cofilin in cell locomotion and invasion. Nat. Rev. Mol. Cell Biol. *14*, 405–415. https://doi.org/10.1038/nrm3609.

69. Garvalov, B.K., Flynn, K.C., Neukirchen, D., Meyn, L., Teusch, N., Wu, X., Brakebusch, C., Bamburg, J.R., and Bradke, F. (2007). Cdc42 Regulates Cofilin during the Establishment of Neuronal Polarity. J. Neurosci. *27*, 13117–13129. https://doi.org/10.1523/JNEUROSCI.3322-07.2007.

70. Dalod, M., Chelbi, R., Malissen, B., and Lawrence, T. (2014). Dendritic cell maturation: functional specialization through signaling specificity and transcriptional programming. EMBO J. *33*, 1104–1116. https://doi.org/10.1002/EMBJ.201488027.

71. Korkmaz, A.G., Popov, T., Peisl, L., Codrea, M.C., Nahnsen, S., Steimle, A., Velic, A., Macek, B., von Bergen, M., Bernhardt, J., and Frick, J.S. (2018). Proteome and phosphoproteome analysis of commensally induced dendritic cell maturation states. J. Proteomics *180*, 11–24. https://doi.org/10.1016/J.JPROT.2017.11.008.

72. Li, R.J.E., de Haas, A., Rodríguez, E., Kalay, H., Zaal, A., Jimenez, C.R., Piersma, S.R., Pham, T.V., Henneman, A.A., de Goeij-de Haas, R.R., et al. (2021). Quantitative Phosphoproteomic Analysis Reveals Dendritic Cell- Specific STAT Signaling After α2-3–Linked Sialic Acid Ligand Binding. Front. Immunol. *12*, 1387. https://doi.org/10.3389/FIMMU.2021.673454/BIBTEX.

73. Hetmanski, J.H.R., de Belly, H., Busnelli, I., Waring, T., Nair, R.V., Sokleva, V., Dobre, O., Cameron, A., Gauthier, N., Lamaze, C., et al. (2019). Membrane Tension Orchestrates Rear Retraction in Matrix-Directed Cell Migration. Dev. Cell *51*, 460–475.e10. https://doi.org/10.1016/J.DEVCEL.2019.09.006.

74. Shen-Orr, S.S., and Furman, D. (2013). Variability in the Immune System: of Vaccine Responses and Immune States. Curr. Opin. Immunol. *25*, 542–547. https://doi.org/10.1016/j.coi.2013.07.009.

75. Ardito, F., Giuliani, M., Perrone, D., Troiano, G., and Lo Muzio, L. (2017). The crucial role of protein phosphorylation in cell signalingand its use as targeted therapy (Review). Int. J. Mol. Med. *40*, 271–280. https://doi.org/10.3892/IJMM.2017.3036/HTML.

76. Kremer, J.R., Mastronarde, D.N., and McIntosh, J.R. (1996). Computer visualization of three-dimensional image data using IMOD. J. Struct. Biol. *116*, 71–76. https://doi.org/10.1006/JSBI.1996.0013.

77. Perez-Riverol, Y., Bai, J., Bandla, C., García-Seisdedos, D., Hewapathirana, S., Kamatchinathan, S., Kundu, D.J., Prakash, A., Frericks-Zipper, A., Eisenacher, M., et al. (2022). The PRIDE database resources in 2022: a hub for mass spectrometry-based proteomics evidences. Nucleic Acids Res. *50*, D543–D552. https://doi.org/10.1093/NAR/GKAB1038.

78. de Vries, I.J.M., Eggert, A.A.O., Scharenborg, N.M., Vissers, J.L.M., Lesterhuis, W.J., Boerman, O.C., Punt, C.J.A., Adema, G.J., and Figdor, C.G. (2002). Phenotypical and functional characterization of clinical grade dendritic cells. J. Immunother. *25*, 429–438. https://doi.org/10.1097/00002371-200209000-00007.

79. Ollion, J., Cochennec, J., Loll, F., Escudé, C., and Boudier, T. (2013). Bioimage informatics TANGO: a generic tool for high-throughput 3D image analysis for studying nuclear organization. Bioinforma. Appl. NOTE *29*, 1840–1841. https://doi.org/10.1093/bioinformatics/btt276.

80. Roos, W.H., Roth, A., Konle, J., Presting, H., Sackmann, E., Spatz, J.P., Otero, F., Grande, H., Rodrìguez, J., Spatz, J.P., et al. (2003). Freely Suspended Actin Cortex Models on Arrays of Microfabricated Pillars. ChemPhysChem *4*, 872–877. https://doi.org/10.1002/CPHC.200300712.

81. Clausen, M.P., Colin-York, H., Schneider, F., Eggeling, C., and Fritzsche, M. (2017). Dissecting the actin cortex density and membrane-cortex distance in living cells by super-resolution microscopy. J. Phys. D Appl. Phys. *50*, 064002. https://doi.org/10.1088/1361-6463/AA52A1.

82. Batth, T.S., Tollenaere, M.X., Rüther, P., Gonzalez-Franquesa, A., Prabhakar, B.S., Bekker-Jensen, S., Deshmukh, A.S., and Olsen, J.V. (2019). Protein Aggregation Capture on Microparticles Enables Multipurpose Proteomics Sample Preparation. Mol. Cell. Proteomics *18*, 1027–1035. https://doi.org/10.1074/MCP.TIR118.001270.

83. Leutert, M., Rodríguez-Mias, R.A., Fukuda, N.K., and Villén, J. (2019). R2-P2 rapid-robotic phosphoproteomics enables multidimensional cell signaling studies. Mol. Syst. Biol. *15*, e9021. https://doi.org/10.15252/MSB.20199021.

84. Bekker-Jensen, D.B., Martínez-Val, A., Steigerwald, S., Rüther, P., Fort, K.L., Arrey, T.N., Harder, A., Makarov, A., and Olsen, J.V. (2020). A Compact Quadrupole-Orbitrap Mass Spectrometer with FAIMS Interface Improves Proteome Coverage in Short LC Gradients. Mol. Cell. Proteomics *19*, 716–729. https://doi.org/10.1074/MCP.TIR119.001906.

85. Bache, N., Geyer, P.E., Bekker-Jensen, D.B., Hoerning, O., Falkenby, L., Treit, P.V., Doll, S., Paron, I., Müller, J.B., Meier, F., et al. (2018). A Novel LC System Embeds Analytes in Pre-formed Gradients for Rapid,

Ultra-robust Proteomics. Mol. Cell. Proteomics *17*, 2284–2296. https://doi.org/10.1074/MCP.TIR118.000853.

86. Bekker-Jensen, D.B., Bernhardt, O.M., Hogrebe, A., Martinez-Val, A., Verbeke, L., Gandhi, T., Kelstrup, C.D., Reiter, L., and Olsen, J.V. (2020). Rapid and site-specific deep phosphoproteome profiling by data-independent acquisition without the need for spectral libraries. Nat. Commun. *11*, 787. https://doi.org/10.1038/S41467-020-14609-1.
87. Tyanova, S., Temu, T., Sinitcyn, P., Carlson, A., Hein, M.Y., Geiger, T., Mann, M., and Cox, J. (2016). The Perseus computational platform for comprehensive analysis of (prote)omics data. Nat. Methods *13*, 731–740. https://doi.org/10.1038/NMETH.3901.
88. Wieczorek, S., Combes, F., Lazar, C., Giai Gianetto, Q., Gatto, L., Dorffer, A., Hesse, A.M., Couté, Y., Ferro, M., Bruley, C., and Burger, T. (2017). DAPAR & ProStaR: software to perform statistical analyses in quantitative discovery proteomics. Bioinformatics *33*, 135–136. https://doi.org/10.1093/BIOINFORMATICS/BTW580.
89. Johnson, W.E., Li, C., and Rabinovic, A. (2007). Adjusting batch effects in microarray expression data using empirical Bayes methods. Biostatistics *8*, 118–127. https://doi.org/10.1093/BIOSTATISTICS/KXJ037.
90. Doncheva, N.T., Morris, J.H., Gorodkin, J., and Jensen, L.J. (2019). Cytoscape StringApp: Network Analysis and Visualization of Proteomics Data. J. Proteome Res. *18*, 623–632. https://doi.org/10.1021/ACS.JPROTEOME.8B00702.
91. Shannon, P., Markiel, A., Ozier, O., Baliga, N.S., Wang, J.T., Ramage, D., Amin, N., Schwikowski, B., and Ideker, T. (2003). Cytoscape: a software environment for integrated models of biomolecular interaction networks. Genome Res. *13*, 2498–2504. https://doi.org/10.1101/GR.1239303.
92. Abraham, M.J., Murtola, T., Schulz, R., Páll, S., Smith, J.C., Hess, B., and Lindahl, E. (2015). GROMACS: High performance molecular simulations through multi-level parallelism from laptops to supercomputers. SoftwareX *1–2*, 19–25. https://doi.org/10.1016/J.SOFTX.2015.06.001.
93. Bussi, G., Donadio, D., and Parrinello, M. (2007). Canonical sampling through velocity rescaling. J. Chem. Phys. *126*, 014101. https://doi.org/10.1063/1.2408420.
94. Berendsen, H.J.C., Postma, J.P.M., Van Gunsteren, W.F., Dinola, A., and Haak, J.R. (1984). Molecular dynamics with coupling to an external bath. J. Chem. Phys. *81*, 3684–3690. https://doi.org/10.1063/1.448118.
95. Huang, J., and Mackerell, A.D. (2013). CHARMM36 all-atom additive protein force field: Validation based on comparison to NMR data. J. Comput. Chem. *34*, 2135–2145. https://doi.org/10.1002/JCC.23354.
96. Huang, J., Rauscher, S., Nawrocki, G., Ran, T., Feig, M., De Groot, B.L., Grubmüller, H., and MacKerell, A.D. (2017). CHARMM36m: an improved force field for folded and intrinsically disordered proteins. Nat. Methods *14*, 71–73. https://doi.org/10.1038/nmeth.4067.
97. Lee, J., Cheng, X., Swails, J.M., Yeom, M.S., Eastman, P.K., Lemkul, J.A., Wei, S., Buckner, J., Jeong, J.C., Qi, Y., et al. (2016). CHARMM-GUI Input Generator for NAMD, GROMACS, AMBER, OpenMM, and CHARMM/OpenMM Simulations Using the CHARMM36 Additive Force Field. J. Chem. Theory Comput. *12*, 405–413. https://doi.org/10.1021/ACS.JCTC.5B00935.
98. Grubmüller, H., Heller, H., Windemuth, A., and Schulten, K. (1991). Generalized Verlet Algorithm for Efficient Molecular Dynamics Simulations with Long-range Interactions. Mol. Simulat. *6*, 121–142. https://doi.org/10.1080/08927029108022142.
99. Darden, T., York, D., and Pedersen, L. (1993). Particle mesh Ewald: An N·log(N) method for Ewald sums in large systems. J. Chem. Phys. *98*, 10089–10092. https://doi.org/10.1063/1.464397.
100. Hess, B., Bekker, H., Berendsen, H.J.C., Fraaije, J.G.E.M., and Fraaije, J.G.E.M. (1997). LINCS: A Linear Constraint Solver for Molecular Simulations. J. Comput. Chem. *18*, 1463–1472.
101. van Rijn, A., Paulis, L., te Riet, J., Vasaturo, A., Reinieren-Beeren, I., van der Schaaf, A., Kuipers, A.J., Schulte, L.P., Jongbloets, B.C., Pasterkamp, R.J., et al. (2016). Semaphorin 7A Promotes Chemokine-Driven Dendritic Cell Migration. J. Immunol. *196*, 459–468. https://doi.org/10.4049/JIMMUNOL.1403096/-/DCSUPPLEMENTAL.

STAR★METHODS

KEY RESOURCES TABLE

REAGENT or RESOURCE	SOURCE	IDENTIFIER
Antibodies		
Cofilin-1	Thermofisher	Cat# MA5-17275; RRID: AB_2538741
Lamin-A/C	Abcam	Cat# ab108595; RRID: AB_10866185
Vimentin	Abcam	Cat# ab92547; RRID: AB_10562134
GAPDH	Cell Signaling	Cat# 2118; RRID: AB_561053
Myosin 9 HC	Thermofisher	Cat# 60233-1-IG; RRID: AB_2881357
Tubulin	Novus Biologicals	Cat# NB100-1639; RRID: AB_10002125
Alexa Fluor™ 647 anti-rabbit	Thermofisher	Cat# A31573; RRID: AB_2536183
Alexa Fluor™ 647 anti-mouse	Thermofisher	Cat# A31571; AB_162542
Alexa Fluor™ 488 anti-rat	Thermofisher	Cat# A11006; RRID: AB_2534074
DC-SIGN	Beckman Coulter	Cat #A07407
CD80	BioLegend	Cat#305214; RRID: AB_528873
CD86	BD Biosciences	Cat #555658; RRID: AB_396013
HLA-DR	BD Biosciences	Cat#559866; RRID: AB_398674
CD11b	Biolegend	Cat#301330; RRID: AB_2561702
Bacterial and virus strains		
XL1 Blue	Gift from Lubbert Dijkhuizen	N/A
Human Peripheral Blood (Buffy Coats)	Sanquin Blood Bank	N/A
Chemicals, peptides, and recombinant proteins		
Lipopolysaccharide	Sigma Aldrich	32160405
Dapi	Sigma Aldrich	32670
Phalloidin Alexa Fluor™ 488	Thermofisher	A12379
Phalloidin Alexa Fluor™ 647	Thermofisher	A22287
IL-4	Miltenyi	130-093-924
GM-CSF	Miltenyi	130-093-867
Formaldehyde	Electron Microscopy Services	15700
Hoechst	Thermofisher	62249
Fetal bovine serum	Thermofisher	10309433
Antibiotic-antimitotic	Gibco	15240062
M-CSF	RnDSystems	216-MC
Collagen I, rat tail	Thermofisher	A1048301
Fibronectin from bovine plasma	Sigma Aldrich	F1141-1MG
Laminin	Merck	L2020
Vitronectin	Peprotech	AF-140-09
Fibrinogen, human type i	Sigma Aldrich	F3879
Cytochalasin D	Merck	C2618
Latrunculin B	Abcam	Ab144291
BODIPY C10	Gift from Ulf Diederichsen[43]	NA
Collagen PureCol Type I Bovine Collagen Solution	Advanced Biomatrix	#5005
α-modified minimal essential medium	Sigma Aldrich	M4526
DQ Gelatin	Thermofisher	D12054
Tris(2-carboxyethyl)phosphine hydrochloride	Merck	C4706
Human Serum	Merck	H4522

(*Continued on next page*)

Continued

REAGENT or RESOURCE	SOURCE	IDENTIFIER
2-Chloroacetamide	Merck	C0267
OptiKlear	Abcam	ab275928
Critical commercial assays		
Polycarbonate membrane filter (1-micron pores)	Sterlitech	PCT1025100
Polycarbonate membrane filter (2-micron pores)	Sterlitech	PCT2013100
Polycarbonate membrane filter (3-micron pores)	Sterlitech	PCT3013100
Micropatterned slides	4D Cell	UM001
Custom-made fibronectin stiffness gels	4D Cell	N/A
Neon™ Transfection System 100 mL Kit Scientific	Thermofisher	MPK10096
Deposited data		
Mass spectrometry data	This paper	PRIDE: PXD031056
Primary microscopy data	This paper	Zenodo: 10571847; https://doi.org/10.5281/zenodo.10571847
Recombinant DNA		
Mini nesprin2 tension sensor	Arsenovic and Conway[34]	RRID: Addgene_68127
Mini nesprin2 tension sensor headless	Arsenovic and Conway[34]	RRID: Addgene_68128
pEGFP-N1 human cofilin-1	Garvalov et al.[69]	RRID: Addgene_50859
pEGFP-N1 human cofilin-1 S3E	Garvalov et al.[69]	RRID: Addgene_50861
pEGFP-N1 human cofilin-1 S3A	Garvalov et al.[69]	RRID: Addgene_50860
pEGFP-N1 human cofilin-1 synthetic (WT)	This study	RRID: Addgene_186747
pEGFP-N1 human cofilin-1 synthetic (S41E)	This study	RRID: Addgene_186748
pEGFP-N1 human cofilin-1 synthetic (S41A)	This study	RRID: Addgene_186749
pmCherry-N1 human cofilin-1 synthetic (WT)	This study	RRID: Addgene_186750
pmCherry-N1 human cofilin-1 synthetic (S41E)	This study	RRID: Addgene_186751
pEGFP-C1 human Lamin A/C	This study	RRID: Addgene_206027
Software and algorithms		
ImageJ/Fiji software	ImageJ	https://imagej.net/software/fiji/
Spectronaut V.15	Biognosys	N/A
Perseus Software v1.6.15.0	Maxquant	https://maxquant.net/perseus/
Prostar online tool	Prostar-proteomics	http://www.prostar-proteomics.org
Cytoscape	Cytoscape	https://cytoscape.org/
GROMACS 2019.3	Gromacs	https://www.gromacs.org/
JPK Data Processing	Bruker	N/A
SymPhoTime 64	PicoQuant	N/A
FLIMfit software 5.1.1.	FLIMfit	https://flimfit.org/
Chemotaxis and Migration Software	Ibidi	https://ibidi.com/chemotaxis-analysis/171-chemotaxis-and-migration-tool.html
Zeiss ZEN software 2.3	Zeiss	N/A
IMOD	Kremer et al.[76]	https://bio3d.colorado.edu/imod/download.html

RESOURCE AVAILABILITY

Lead contact

Further information and requests for resources and reagents should be directed to and will be fulfilled by the Lead Contact, Geert van den Bogaart (g.van.den.bogaart@rug.nl).

Materials availability

All plasmids have been deposited to Addgene.

Data and code availability

- All raw MS data were generated by the authors and deposited to the ProteomeXchange Consortium (http://proteomecentral.proteomexchange.org) via the PRIDE partner repository[77] with the dataset identifier PXD031056. Primary microscopy data generated in this study have been deposited in the Zenodo database under accession code https://doi.org/10.5281/zenodo.10571847.
- Our macro for measuring ratiometric FRET is available to readers upon request.
- Any additional information required to reanalyze the data reported in this work paper is available from the lead contact upon request.

EXPERIMENTAL MODEL AND STUDY PARTICIPANT DETAILS

Monocyte-derived dendritic cells were obtained by differentiating monocytes with interleukin (IL)-4 (300 μg/ml) and granulocyte-macrophage colony-stimulating factor (GM-CSF; 450 μg/ml) for 6 days in RPMI supplemented with 10% serum, antibiotics (100 μg ml^{-1} penicillin, 100 μg ml^{-1} streptomycin and 0.25 μg ml^{-1} amphotericin B, Gibco), and 2 mM glutamine. Monocytes were isolated from the blood of healthy donors (informed consent and consent to publish obtained, approved by the ethical committee of Dutch blood bank Sanquin) as previously described.[78] LPS (O111:B4, Sigma Aldrich 32160405) stimulation was carried out overnight unless otherwise stated.

$CD14^+$ macrophages were obtained as previously described. In brief $CD14^+$ monocytes were isolated using MACs kits (Miltenyi) from the blood of healthy donors. The $CD14^+$ monocytes were differentiated for 7 days on low-adherence plates (Corning) in RPMI supplemented with 10% serum, antibiotics (100 μg ml^{-1} penicillin, 100 μg ml^{-1} streptomycin and 0.25 μg ml^{-1} amphotericin B, Gibco), and M-CSF (100ng/ml) for 7 days.

METHOD DETAILS

Reagents antibodies

The following primary antibodies were used in this study: cofilin-1 (Thermofisher GT567, 1:200): 1:200, lamin-A/C (Abcam ab108595, 1:200 for immunofluorescence, 1/1000 for western blot), vimentin (Abcam ab92547, 1:200), tubulin (Novus Biologicals YOL1/34), GAPDH (Cell Signaling 2118, 1:500), Myosin 9 HC (Thermofisher 5D9D2, 1:200).

The following secondary antibodies and reagents were for immunofluorescence: donkey anti-rabbit 647 (Thermo Fisher A31573), goat anti-rat 488 (Thermo Fisher A11006), donkey anti-mouse 647 (Thermo Fisher A31571), phalloidin Alexa-Fluor-488 (Thermo Fisher A12379), phalloidin Alexa-Fluor- 647 (Thermo Fisher A22287), DAPI (Sigma Aldrich 32670).

Total cell lysis and western blotting

Total cell lysates were obtained using a boiling SDS lysis buffer (5% sodium dodecyl sulfate (SDS), 5 mM tris (2-carboxy- ethyl)phosphine (TCEP), 10 mM chloroacetamide (CAA), 100 mM Tris, pH 8.5). Lysates were then incubated for 10 minutes at 95°C. Lysates were resolved on polyacrylamide gels and transferred to methanol-activated PVDF. Blots were scanned with an Odyssey XF imaging system (LI-COR Biosciences).

Confocal microscopy

Cells were seeded onto glass coverslips for at least 12 hours before fixation. Cells were fixed in 4% PFA for 15 minutes at room temperature, or ice-cold methanol for 10 minutes at -20°C (for lamin-A/C immunolabeling). Cells fixed in PFA were permeabilized for 5 minutes in a 0.1% (v/v) Triton-X100 solution. Cells were blocked in a 20 mM glycine 3% BSA PBS-based solution for 1 hour before antibody staining.

Transient transfection of dendritic cells was achieved using the Neon-transfection system (Thermo Scientific). In brief, 1.2 million cells were washed with PBS and suspended in 115 μL of buffer R with 5 μg of DNA. Cells were pulsed twice for 40 ms at 1000 V. Cells were then transferred to phenol red-free RPMI with 20% serum for at least 4 hours before imaging. Live cell imaging was performed in OptiKlear solution (Abcam ab275928).

Images were collected with a Zeiss LSM 800 microscope equipped with a Plan-Apochromat (63x/1.4) oil DIC M27 (FWD=0,19 mm) objective (Zeiss). Images were acquired using the ZEN software (version 2.3). DAPI was excited by a 405 laser, and Alexa Fluor 488 phalloidin was excited by a 488 laser. For Z-series, a slice interval of 0.31 μm was used. Airyscan microscopy was performed with a Zeiss LSM 800 airyscan microscope. A Z-interval of 0.17 μm was used. Images were acquired using the ZEN software (version 2.3). Images were subject to airyscan processing following acquisition. 3D reconstruction was achieved using the IMOD software package.[76] Nuclear sphericity was analysed using the 3D Image J Suite.[79]

ECM coating of glass coverslips

Sterile glass coverslips were coated in a PBS solution containing each respective ECM protein (collagen (0.3 mg ml^{-1}), fibronectin (33 μg ml^{-1}), laminin (0.1-0.2 mg ml^{-1}), vitronectin (0.1 mg ml^{-1}), fibrinogen (0.1 mg ml^{-1})) overnight. The coverslips were then washed with PBS before the seeding of dendritic cells in RPMI supplemented with serum and antibiotics.

Inhibitors

Cytochalasin D (Merck C2618) was used at concentrations ranging from 100nM to 10 μM, Latrunculin B (Abcam Ab144291) was used at 100nM. All inhibitors were added for 1 hour.

Bodipy-C10

The BODIPY C10 dye (kind gift from Dr. Ulf Diederichsen, Georg-August-Universität Göttingen, Germany) was used at 4 μM to stain cells for 30 minutes before imaging. Cells were then washed twice with phenol-red free RPMI before imaging. Cells were imaged using a PicoQuant MicroTime 200 microscope equipped with an Olympus (100x/1,4) oil immersion objective. Images were acquired using the SymPhoTime 64 software. Data analysis of FLIM images was performed using the open-source FLIMfit software (version 5.1.1.). For analyzing the nuclear membrane, parts of the respective membrane were selected to avoid adjacent organelles.

Atomic force microscopy

AFM measurements were performed using a commercial JPK NanoWizard mounted on an inverted optical microscope (Olympus). The AFM was equipped with a JPK Biocell heated stage and the measuring temperature was kept at a constant 37°C. Silicon nitride cantilevers with a triangular pyramidal probe and a nominal spring constant of 0.1 N/m were used (MLCT-BIO E, Bruker). The cells were seeded on clean glass coverslips. Cell nuclei were identified through light microscopy and then imaged in Quantitative Imaging mode before indenting. Indentations were performed by drawing a 6x6 points grid in a 3x3 μm area on the highest point of the nucleus and then indenting each point once, after which moving on to a different cell. Indentations were performed to a set-point of 1 nN at a velocity of 1 μm/s. In between cells, a glass curve was taken to check for tip contamination.

Both image and force curves were processed using JPK Data Processing software. Curves were fit using the inbuilt Hertz / Sneddon model for triangular pyramid-shaped probes to obtain the Young's modulus. In Figure 4I each data point corresponds to a single indentation of the used 6x6 grid. Batch processing was used with manually chosen fitting ranges. Typical deformation of the cells at the place of the nucleus was ~1.5 μm. This indicates that the indentation was much deeper than the actin cortex layer which is several hundreds of nanometer thick[80,81] and that a considerable part of the nucleus was deformed.

FLOW CYTOMETRY

Monocyte-derived dendritic cells and monocytes isolated with the CD14 MACS kit from Miltenyi biotec (130-050-201) were collected in a V-bottom plate at 10^5 cells/well (Thermo scientific # 10462012) and pelleted (300 *xg*, 3 min, 4°C). Next, cells were blocked in 2% human serum and PBS for 30 min at 4°C and stained with fluorescently labeled antibodies raised against DC-SIGN (Beckman Coulter #A07407), CD80 (BioLegend #305214), CD86 (BD #555658) and HLA-DR (BD #559866) After staining, the cells were washed in PBS two times, and recorded on a CytoFlex S flow cytometer (Beckman Coulter), and analysed with FlowJo.

Plasmids

The following plasmids were used in this study: mN2G-TS (gift from Daniel Conway; Addgene 68127),[34] pcDNA nesprin HL (gift from Daniel Conway; Addgene 68128) , pEGFP-N1 human cofilin-1 WT (gift from James Bamburg; Addgene 50859), pEGFP-N1 human cofilin-1 S3E (gift from James Bamburg; Addgene 50861), pEGFP-N1 human cofilin-1 S3A (gift from James Bamburg; Addgene 50860) cofilin-1.[69] pEGFP-N1 human cofilin-1 1 S41A and pEGFP-N1 cofilin-1 S41E, and pEGFP-C1 Lamin A/C (*LMNA*) were generated as synthetic genes (Genscript) and have been deposited at Addgene.

Ratiometric FRET analysis

Ratiometric FRET images were analysed using an in-house ImageJ macro. The macro divides the YFP-FRET signal by the sum of the YFP-FRET and CFP signal. Our macro is available to readers upon request.

3D cell culture

Custom-made fibronectin stiffness gels were purchased from 4D Cell. Cells were cultured overnight in corning plastic in the presence or absence of LPS, at 37°C, 5% CO_2. Cells were then detached via incubation in PBS at 4°C and re-seeded onto stiffness gels, before being allowed to adhere for at least 3 hours before fixation with PFA. Cells were then stained with phalloidin and DAPI, and imaged using confocal microscopy.

Collagen matrix was generated using a PureCol Type I Bovine Collagen Solution (Advanced Biomatrix; #5005), α-modified minimal essential medium (Sigma Aldrich; M4526) and sodium bicarbonate. Collagen mixture was allowed to pre-polymerise for 5 minutes at 37 °C prior to adding a 45 μl cell suspension containing 60,000 moDCs expressing either WT or mutant cofilin in phenol red-free RPMI. The total mixture was transferred to a 96-well black plate (Greiner Bio-One; 655090) and incubated for 45 minutes at 37°C. Afterwards, phenol red–free RPMI 1640 culture medium supplemented with 1 % ultraglutamine and 10 % FBS was added on top of the matrices.

Micropatterned substrate

Micropatterned slides were purchased from 4D Cell (UM001 – squares and discs). Cells were allowed to adhere on the slides prior to being 4% PFA for 15 minutes. Samples were then stained with DAPI and phalloidin, mounted and imaged.

Gelatin impregnated filters

Polycarbonate membrane filters (Sterlitech, Kent, WA: PCT1025100 – 1-micron pores, PCT2013100 – 2-micron pores, PCT3013100 – 3-micron pores) were washed with 70% ethanol before being pressed between a glass coverslip and a parafilm sheet, with a droplet of fluorescent gelatin (DQ Gelatin – Thermo D12054) for 10 minutes. The membranes were then washed with PBS before cells were seeded on top of the membrane filter. Following overnight incubation, samples were fixed in 4% PFA for 15 minutes. Samples were then stained with DAPI and phalloidin, mounted and imaged.

Invasion was calculated by normalizing the total number of cells on the underside of filters to the seeding density on the topside of the filters. This was then normalized for the +LPS condition to the –LPS condition.

Cell lysis and digestion for proteomics analysis

Cells were lysed in boiling 5% SDS buffer (in 100 mM Tris-HCl pH 8.5, 5 TCEP, 10 mM CAA). Lysates were heated for 10 minutes. After sonication, protein concentration was estimated by BCA assay (Pierce). Protein digestion using the PAC method[82] was automated on a KingFisher™ Flex robot (Thermo Fisher Scientific) in 96-well format, as previously described.[83,84] The 96-well comb is stored in plate #1, the sample in plate #2 in a final concentration of 70% acetonitrile and with magnetic amine beads (ReSyn Biosciences) in a protein/bead ratio of 1:2. Washing solutions are in plates #3–5 (95% Acetonitrile) and plates #6–7 (70% Ethanol). Plate #8 contains 300 μl digestion solution of 50 mM ammonium bicarbonate (ABC), LysC in an enzyme/protein ratio of 1:500 (w/w) and trypsin in an enzyme:protein ratio of 1:250. The protein aggregation was carried out in two steps of 1 min mixing at medium mixing speed, followed by a 10 min pause each. The sequential washes were performed in 2.5 min and slow speed, without releasing the beads from the magnet. The digestion was set to 12 h at 37 °C with slow speed. After overnight digestion, enzymatic activity was quenched by acidifying the lysates using trifluoroacetic acid (TFA) at a final concentration of 1% and ensuring the pH of the samples being around 2. Digested peptides for single-shot proteome analysis were loaded directly on C18 evotips (Evosep) for MS analysis. Digested peptides for phosphoproteomics were purified and concentrated on reversed-phase C18 Sep-Pak cartridges (Waters). After elution with 40% acetonitrile (ACN) followed by 60% ACN, a SpeedVac concentrator (ThermoFisher Scientific), operating at 60°C, was utilized to concentrate the samples. Peptide concentration was estimated by measuring absorbance at A280 on a NanoDrop spectrophotometer (ThermoFisher Scientific).

Enrichment of phosphorylated peptides

Ti-IMAC phosphopeptide enrichment was carried out on a KingFisher™ Flex robot (Thermo Fisher Scientific) in 96-well format, as previously described.[84] 200 μg of peptide were used for enrichments, with 20 μl of magnetic Ti-IMAC HP beads (ReSyn Biosciences). The 96-well comb is stored in plate #1, Ti-IMAC HP beads in 100% ACN in plate #2 and loading buffer (1 M glycolic acid, 80% ACN, 5% TFA) in plate #3. The sample is mixed with loading buffer and added in plate #4. Plates 5–7 are filled with 500 μl of washing solutions (loading buffer, 80% ACN, 5% TFA, and 10% ACN, 0.2% TFA, respectively). Plate #8 contains 200 μl of 1% NH4OH for elution. The beads are washed in loading buffer for 5 minutes at medium mixing speed, followed by binding of the phosphopeptides for 20 minutes and medium speed. The sequential washes are performed in 2 minutes and fast speed. Phosphopeptides are eluted in 10 minutes at medium mixing speed. After acidification, phosphopeptides were loaded directly on C18 evotips (Evosep) for MS analysis.

Liquid chromatography-tandem mass spectrometry

Label-free proteome and phosphoproteome samples were analyzed on the Evosep One system[85] coupled to an Orbitrap Exploris 480.[84] Samples were separated on an in-house packed 15 cm analytical column (150 μm inner diameter), packed with 1.9 μm C18 beads, and column temperature was maintained at 60 °C using an integrated column oven (PRSO-V1, Sonation GmbH). Preprogrammed gradients were used: 30 samples per day for proteome, 60 samples per day for phosphoproteome. The mass spectrometer was operated in positive ion mode, using data-independent acquisition (DIA), as previously described,[86] with spray voltage at 2 kV, heated capillary temperature at 275 °C and funnel RF frequency at 40. Full MS resolution was set to 120,000 at m/z 200 and full MS AGC target was 300%, with an injection time of 45 ms, and scan range was set to 350–1400 m/z. AGC target value for fragment scan was set at 1000%. 49 windows of 13.7 Da were used with an overlap of one Da. The MS/MS acquisition was set to 15,000 resolution, and injection time to 22 ms. Normalized collision energy was set at 27%. Peptide match was set to off, and isotope exclusion was on.

Mass spectrometry raw data processing

Data were analyzed on Spectronaut V.15 in directDIA mode (spectral library-free) with the standard settings. For phosphoproteome analysis, the PTM localization filter was set at 0.75. Deamidation of asparagine and glutamine (NQ) was added as variable

modification for both proteome and phosphoproteome data, and phosphorylation of serine, threonine and tyrosine (STY) only for the phosphoproteome data. The Human Uniprot fasta file (downloaded in 2019, 21,074 entries) was supplemented with a contaminant fasta files containing 246 entries.

Bioinformatic analysis

Data analysis was done the Perseus Software[87] v1.6.15.0 and the Prostar online tool (http://www.prostar-proteomics.org/).[88] Plots in Figures 5 and S4 were performed using the ggplot2 package v3.3.5, using the R software package v4.1.1 (with RStudio v1.2.5042).

Proteome data

Protein group MS intensities were Log2-transformed and filtered by removing potential contaminants, rows without gene name and with less than 4 valid values in at least one condition (Ctrl, 1h or 4h). Data normalization was performed by variance stabilization normalization (VSN) as implemented in Prostar. Missing values were imputing by using the R plugin imputeLCMD (https://cran.rstudio.com/web/packages/imputeLCMD/index.html) as implemented in Perseus (QRILC = 1). Inter-patient batch effect was removed by using the R plugin Combat[89] as implemented in Perseus. Principal component analysis (PCA) was performed in Perseus on normalized, imputed and batch-corrected data. Differential expression analysis was performed in Perseus by using one-way ANOVA. p values were corrected by using the Benjamini–Hochberg (BH) procedure. Proteins were considered significantly regulated if p adjusted was < 0.01. Gene ontology (GO) and pathway (KEGG and Reactome) enrichment analyses were performed in Perseus by Fisher exact test against the whole dataset as background. p values were corrected by using the BH procedure. Hierarchical clustering of protein group intensities was performed in Perseus after row scaling (Z-score) by using Pearson correlation.

Phosphoproteome data

Phosphosite MS intensities were Log2-transformed and filtered by removing potential contaminants and phosphorylation sites with less than 4 valid values in at least one condition (Ctrl, 1h or 4h). The ''expand the site table'' function, implemented in Perseus, was used. MS intensities were normalized in Spectronaut. Missing value imputation (QRILC1.3), batch effect removal, one-way ANOVA, GO/pathway enrichment analysis and hierarchical clustering were performed as described above for the proteome. Phosphosites were filtered based on their functional score with a cutoff of 0.45.[48] Functional protein network analysis was performed in STRING[49] through the STRING App[90] implemented for the Cytoscape software.[91] Network analysis (calculation of degree and closeness centrality) was performed in Cytoscape.

Molecular modeling: General simulation details

All simulations were performed with GROMACS 2019.3[92] at a 0.18 M NaCl salt concentration. Systems were kept at a constant temperature using a velocity rescaling thermostat[93] (τ_T = 1 ps). Pressure coupling was performed with the Berendsen barostat[94] (τ_T = 2 ps, $4.5 \cdot 10^{-5}$ compressibility and 1 bar reference pressure).

Molecular modeling: All-atom replica exchange MD

All-atom molecular dynamics simulations were performed with the February 2021 version of the CHARMM36 force field[95,96] with a 2 fs time step. The cofilin-1 NMR structure was downloaded from the PDB (entry 1tvj) and phosphorylated at Ser3 and Ser41 with the Charmm GUI.[97] Protein structures were solvated in tip3p water and the systems were neutralized with additional Na^+ or Cl^- ions. After the steepest descent minimization, the systems were equilibrated for 10 ns at 48 different temperatures, ranging from 310 to 427.5 K, with steps of 2.5 K. With these 48 equilibrated systems, replica-exchange runs were performed for 50 ns, with an exchange attempt every 500 steps. Van der Waals and Coulomb interactions were calculated using the shifted Verlet[98] and particle mesh Ewald (PME)[99] methods, respectively, both with a 1.2 nm cut-off distance. The LINCS algorithm[100] was used to constraint bonds with hydrogen atoms. For analysis, the trajectories were de-multiplexed using GROMACS' demux.pl script to obtain trajectories with continuous coordinates.

Time-lapse microscopy

Day 6 moDCs were transfected with GFP-WT cofilin or mCherry-labelled mutant cofilin using a Neon electroporator (Thermofisher Scientific). moDCs were pulsed twice at 1000 V for 40 ms and using 10 μg of the corresponding plasmid. After transfection cells were immediately incubated at 37°C for 4 h in phenol red-free RPMI 1640 containing 10 % FBS and 1 % ultra-glutamine prior to being sorted using a FACS Melody WT or mutant cofilin expressing cells were then embedded into a collagen matrix with a final concentration of 1.7 mg ml^{-1}.

Time lapsed video microscopy was performed using the Zeiss Axio Observer 7 with Zeiss Axiocam 702 camera, Sutter Lambda DG5 light source, fast filter wheels, Zen image acquisition and analysis software and Ibidi stage incubator. Sequential images were taken every 5 min using an LD Plan-Neofluar 20x /0.4 Korr M27 GFP-WT cofilin expressing cells were excited with a 488 laser and mCherry-labeled mutant cofilin cells with a 592 laser.

Individual cell tracking was performed to determine the median cell velocity, the cell mean square displacement (MSD) and the Euclidean distance reached by a cell after 120 minutes of tracking. Cell tracking was performed 4 hours after embedding cells in the collagen to allow adaptation to the environment and using the manual tracking plugin of Fiji (ImageJ) with adjusted

microscope-specific time and calibration parameters. Cells were chosen randomly and dead cells were excluded from the cell tracking. The MSD over time intervals was determined as described in the protocol of Van Rijn et al.[101] In short, the MSD was calculated per time interval for each cell. The average per time interval was calculated for all cells corrected for the tracking length of the cells. The Euclidean distance was calculated using the Chemotaxis and Migration software (Ibidi).

QUANTIFICATION AND STATISTICAL ANALYSIS

Statistical comparisons were made with GraphPad Prism 8 software, and data expressed as described in the figure legends (2-sides unpaired t-test, Mann-Whitney U Test, ANOVA/Tukey multiple comparison test, Kolmogorov-Smirnov test). Statistical significance was determined as $p \leq 0.05$